



Powerful Explosions from the Collapse of Rotating Supermassive Stars

Sho Fujibayashi^{1,2,3} , Cédric Jockel³ , Kyohei Kawaguchi^{3,4,5} , Yuichiro Sekiguchi^{5,6} , and Masaru Shibata^{3,5} ¹ Frontier Research Institute for Interdisciplinary Sciences, Tohoku University, Sendai 980-8578, Japan; sho.fujibayashi@astr.tohoku.ac.jp² Astronomical Institute, Graduate School of Science, Tohoku University, Sendai 980-8578, Japan³ Max-Planck-Institut für Gravitationsphysik (Albert-Einstein-Institut), Am Mühlenberg 1, D-14476 Potsdam-Golm, Germany⁴ Institute for Cosmic Ray Research, The University of Tokyo, 5-1-5 Kashiwanoha, Kashiwa, Chiba 277-8582, Japan⁵ Center for Gravitational Physics and Quantum Information, Yukawa Institute for Theoretical Physics, Kyoto University, Kyoto, 606-8502, Japan⁶ Department of Physics, Toho University, Funabashi, Chiba 274-8510, Japan

Received 2024 August 21; revised 2025 January 28; accepted 2025 January 29; published 2025 March 4

Abstract

We perform new general relativistic hydrodynamics simulations for collapses of rotating supermassive star cores with an approximate nuclear burning up to carbon and a detailed equation of state. For all the models we investigate, the energy generation by nuclear burning plays only a minor role, leading to the formation of a black hole without a nuclear-powered explosion. For rotating models, however, the stellar explosion associated with shock heating is driven from a torus, which forms after the black hole formation. The explosion energy is up to 10^{-4} of the mass energy of the supermassive star cores ($\sim 10^{55}$ – 10^{56} erg). We find that, even if we increase the rotational angular momentum of the progenitor, the ejecta mass saturates at $\sim 1\%$ of the total mass of the initial stellar core. The average ejecta velocity also saturates at $\approx 20\%$ of the speed of light. As a result, the ejecta kinetic energy is approximately proportional to the initial mass of the supermassive star core for the rapidly rotating case. We also perform viscous hydrodynamics simulations to explore the evolution of the remnant torus. Although the viscous heating drives an outflow from the torus, we find that its effect is subdominant in terms of the kinetic energy because of the small velocity ($\approx 0.07c$) of the ejecta component.

Unified Astronomy Thesaurus concepts: [Supermassive black holes \(1663\)](#); [Massive stars \(732\)](#); [Gravitational collapse \(662\)](#)

1. Introduction

The presence of supermassive black holes with estimated high masses of $\sim 10^7$ – $10^{10}M_{\odot}$ in the early universe is an intriguing puzzle. The recent extensive searches for high-redshift galaxies indicate that a number of supermassive black holes of mass $\gtrsim 10^9M_{\odot}$ were already present in the first billion years ($z \gtrsim 6$) after the Big Bang (e.g., X. Fan et al. 2023; A. D. Goulding et al. 2023; Á. Bogdán et al. 2024; O. E. Kovács et al. 2024). This suggests that rapid growth of the black holes from their massive or very massive seeds is required in the early universe (e.g., K. Inayoshi et al. 2020; M. Volonteri et al. 2021 for reviews).

The growth of the black hole mass is typically limited by the Eddington rate. In this respect, a high mass of the seed black holes is preferred for the swift formation of supermassive black holes. For example, the seed black holes may originate from collapses of ~ 100 – $1000M_{\odot}$ Population III stars, as indicated in numerical simulations (S. Hirano et al. 2014). To reach a 10^9M_{\odot} black hole from one with 10^3M_{\odot} by $z = 6$, a mass accretion rate with nearly Eddington rate is required throughout its growing history of about 1 billion yr. However, several feedback effects, which can stem from, e.g., radiation pressure during the mass accretion onto the seed black hole and nearby supernova explosions (J. L. Johnson & V. Bromm 2007; D. Whalen et al. 2008;

M. A. Alvarez et al. 2009; M. Milosavljević et al. 2009), could make such a high duty cycle unlikely.⁷

Several scenarios have been proposed for the formation of a high-mass seed black hole (e.g., M. J. Rees 1978; K. Inayoshi et al. 2020; M. Volonteri et al. 2021). One of the scenarios is the so-called direct collapse scenario (e.g., V. Bromm & A. Loeb 2003). In this scenario, a supermassive star with a mass of $\sim 10^4$ – 10^6M_{\odot} is formed in a rapidly accreting (with a mass accretion rate of $\sim 0.1M_{\odot}\text{yr}^{-1}$) high-temperature primordial gas cloud, which is cooled primarily by atomic hydrogen line emissions⁸ (e.g., L. Mayer & S. Bonoli 2019; and M. Gieles et al. 2018 for other formation scenarios of supermassive stars). The supermassive star then collapses to a massive black hole due to the general relativistic instability (S. Chandrasekhar 1964). The resulting large initial mass of the seed black hole helps to grow to a supermassive black hole in a shorter timescale. Therefore, the collapse of supermassive stars is one of the most promising scenarios for the formation of the supermassive black hole seeds in the early universe.

Supermassive stars may not just collapse into a black hole but show some astrophysical transients. It was shown that an explosion is possible due to the energy generation by nuclear

⁷ There is a possibility of the mass accretion exceeding the Eddington limit (super- or hyper-Eddington accretion) if the mass accretion rate of the black hole is so high that photons are trapped in the accretion flow. This growth path of a black hole may be possible if the black hole is embedded in a dense region (e.g., K. Inayoshi et al. 2020 and references therein).

⁸ The gas cloud that hosts a supermassive star should lack molecular hydrogen due to, e.g., strong irradiation of far-ultraviolet photons (K. Omukai 2001), collisional dissociation in a dense and hot region that experienced a strong shock (K. Inayoshi & K. Omukai 2012), or mechanical heating by frequent merger of the host halos (S. Chon et al. 2016; S. Hirano et al. 2017; J. H. Wise et al. 2019; D. Toyouchi et al. 2023).

burning. K. J. Fricke (1973), G. M. Fuller et al. (1986), and P. J. Montero et al. (2012) demonstrated that a supermassive star could explode by hydrogen burning via the carbon–nitrogen–oxygen (CNO) cycle if the supermassive star is metal rich. More recently, K.-J. Chen et al. (2014a), C. Nagele et al. (2020, 2022, 2023a), and C. Nagele & H. Umeda (2024) showed that the explosion is possible also by the explosive helium burning.

The rotation of the star may also play an important role in inducing the explosion. If a supermassive star is rapidly rotating, the star not only collapses into black holes but also forms a torus surrounding the black hole. In this case, further activities can be expected, because the torus formation process can be accompanied by strong shock-wave formation that subsequently drives a powerful outflow of unbound matter (W. H. Lee & E. Ramirez-Ruiz 2006; Y. T. Liu et al. 2007; H. Uchida et al. 2017). In addition, the effective viscosity induced by the magnetohydrodynamical processes in the torus could drive a postcollapse outflow from it. The black hole–torus system may also drive a relativistic outflow (T. Matsumoto et al. 2015) if a magnetosphere is developed along the rotational axis of the formed black hole.

Massive stars with nearly Eddington luminosity have a smaller breakup surface velocity than the Keplerian velocity (A. Maeder & G. Meynet 2000). Based on recent stellar evolution simulations, it is speculated that the accreted angular momentum should be significantly smaller than that of the Keplerian value in order not to exceed the breakup velocity by the accretion (e.g., H. Lee & S.-C. Yoon 2016; L. Haemmerlé et al. 2018). However, current studies on the rotation of supermassive stars are limited by their assumption of spherical symmetry. A recent multidimensional simulation (K. Kimura et al. 2023) suggests that supermassive protostars can have an oblate shape, enabling them to rotate at nearly half their breakup speed when their mass reaches $10M_{\odot}$. If this shape persists as the star gains more mass, it could lead to faster rotation than current stellar evolution models predict. Further simulations at higher masses are needed to confirm this possibility.

Explosions of supermassive stars induce astronomical transient events. The formation and collapse of supermassive stars are likely to occur in the high-redshift universe at $z \sim 10$. The observations of such early universe are rapidly progressing, especially with the James Webb Space Telescope (JWST). The event rate of the transient induced by the collapse of supermassive stars began to be constrained (T. J. Moriya et al. 2023).

Motivated by the above considerations, we revisit the collapse of rotating supermassive star cores in this paper. We focus, in particular, on the properties of the matter ejected as a result of the explosive shock heating at the formation of a torus. For this purpose, we first perform a set of new axisymmetric fully general relativistic hydrodynamics simulations starting from equilibrium configurations of supermassive star cores that are subject to general relativistic instability. In these simulations, we take into account the effect of hydrogen burning and triple- α reactions in a simple, but consistent way. We further perform a viscous hydrodynamics simulation for the remnant torus to investigate the effect of the postcollapse mass ejection, assuming a hypothetical enhancement of the effective viscosity that can be developed in the presence of a magnetohydrodynamical turbulence (S. A. Balbus & J. F. Hawley 1998).

This paper is organized as follows: In Section 2, we present the numerical methods used in the present simulation. Then, in Section 3, the results are described, focusing on the properties of the ejecta. We discuss a possible astrophysical transient based on our results in Section 4. Finally, Section 5 is devoted to a summary. Throughout this paper, G , c , and k_B denote the gravitational constant, speed of light, and Boltzmann’s constant, respectively.

2. Method

A general relativistic neutrino radiation hydrodynamics code is employed for the simulations. Einstein’s equations are solved with a version of the puncture-Baumgarte–Shapiro–Shibata–Nakamura formalism (M. Shibata & T. Nakamura 1995; T. W. Baumgarte & S. L. Shapiro 1998; M. Campanelli et al. 2006) with a Z4c constraint propagation scheme (D. Hilditch et al. 2013). The so-called cartoon method (M. Shibata 2000; M. Alcubierre et al. 2001; M. Shibata & Y. Sekiguchi 2012) is used to impose the axial symmetry. The basic method of radiation hydrodynamics is the same as that in our previous studies (e.g., Y. Sekiguchi 2010; S. Fujibayashi et al. 2017, 2020c). To account for the energy generation by nuclear burning, the mass fractions of several nuclear species are evolved. Neutrino radiation transport is taken into account with an energy-integrated truncated moment formalism (K. S. Thorne 1981; M. Shibata et al. 2011). In the supermassive star collapse, the optical depth of the matter to neutrinos is always much lower than unity, and hence, the neutrino process simply acts as cooling.

2.1. Radiation Hydrodynamics

The evolution of the energy and momentum densities of the fluid and neutrino radiation is described in a covariant way by

$$\nabla_{\alpha} T_{(\text{fl})}^{\alpha\mu} = -S_{\mu}, \quad (1)$$

$$\nabla_{\alpha} T_{(\nu)}^{\alpha\mu} = +S_{\mu}, \quad (2)$$

where $T_{(\text{fl})}^{\alpha\mu}$ and $T_{(\nu)}^{\alpha\mu}$ are the energy-momentum tensors of the fluid and neutrino radiation, respectively, and ∇_{α} denotes the covariant derivative.⁹ S_{μ} denotes the source term due to neutrino emission, and the total energy-momentum tensor, $T_{\mu}^{\alpha} = T_{(\text{fl})}^{\alpha\mu} + T_{(\nu)}^{\alpha\mu}$, satisfies the local energy-momentum conservation $\nabla_{\alpha} T_{\mu}^{\alpha} = 0$. We note that there is no direct source term for the fluid (right-hand side of Equation (1)) that describes the heating by nuclear burning. The nuclear heating effect is reflected as a result of the increase of the internal energy due to the mass defect (see Section 2.4). We solve Equations (1) and (2) in the same scheme as described in S. Fujibayashi et al. (2017).

2.2. Nuclear Burning

In addition to the usual hydrodynamical variables, mass fractions of several nuclear species are solved. Here, we summarize the basic equations that govern their evolution.

⁹ Throughout this paper, Greek and Latin indices (except for I) run over spacetime and space coordinates, respectively. The subscript I denotes a species of particles.

2.2.1. Basic Equation

The equation for the number density of a nuclear species, n_I , is written in a covariant way as

$$\nabla_\mu(n_I u^\mu) = \dot{n}_I|_{\text{reac}}, \quad (3)$$

where u^μ is the common four velocity of the fluid, and $\dot{n}_I|_{\text{reac}}$ is the change rate in the number density of the I th nuclear species in the fluid rest frame. We define a mass fraction $X_I = A_I n_I / n_b$, where A_I is the mass number of the I th species, and n_b is the baryon number density. Then, Equation (3) is rewritten to the evolution equation for the mass fraction as

$$\partial_\mu(\sqrt{-g} \rho X_I u^\mu) = A_I m_u \sqrt{-g} \dot{n}_I|_{\text{reac}}, \quad (4)$$

where g is the determinant of the spacetime metric, and m_u is the atomic mass unit, and $\rho = m_u n_b$ is the rest-mass density.

Following H. Uchida et al. (2017) and P. J. Montero et al. (2012), we consider the CNO cycle of the hydrogen burning and triple- α reaction of the helium burning for the relevant energy-generation processes. We thus consider only three nuclear species, ^1H , ^4He , and ‘‘CNO species,’’ which are denoted by subscripts p , α , and CNO, respectively. The ‘‘CNO species’’ denotes the total species that catalyze the CNO cycle (isotopes of carbon, nitrogen, and oxygen). The right-hand side of Equation (4) is calculated so that the energy-generation rate of each reaction becomes consistent with that in P. J. Montero et al. (2012).

2.2.2. CNO Cycle

For temperatures of $T \gtrsim 1 \times 10^7$ K, the CNO cycle dominates the hydrogen burning. The CNO cycle in a low-temperature region is called cold CNO cycle, which is what we find in the context of hydrostatic stellar nucleosynthesis. The number in the cold CNO cycles that occur per unit time per unit volume is described as

$$\begin{aligned} \dot{n}_{\text{cCNO}} &= \frac{\rho \epsilon_{\text{cCNO}}}{Q_{\text{cCNO}}} \\ &= 1.1 \times 10^{30} \text{ cm}^{-3} \text{ s}^{-1} \rho^2 X_p X_{\text{CNO}} \\ &\quad \times [T_9^{-2/3} \exp(-15.231 T_9^{-1/3}) \\ &\quad + 8.3 \times 10^{-5} T_9^{-3/2} \exp(-3.0057 T_9^{-1})], \end{aligned} \quad (5)$$

where $T_9 := T/(10^9 \text{K})$, and X_p and X_{CNO} are mass fractions of ^1H and CNO species. Equation (5) is derived from the expression in K. J. Shen & L. Bildsten (2007) and M. Wiescher et al. (1999) with the liberated energy $Q_{\text{cCNO}} = (26.73 - 0.71 - 1.00) \text{ MeV}$, which is the difference of the masses of four ^1H and one ^4He with the subtraction of the average energies of two neutrinos emitted by beta decays of ^{13}N and ^{15}O (the values are taken from the Evaluated Nuclear Data File database¹⁰).

The hot CNO cycle is the dominant process if the timescale of the reaction $^{13}\text{N}(p, \gamma)^{14}\text{O}$ is shorter than that of $^{13}\text{N}(e^+ \nu_e)^{13}\text{C}$ (the half-life is approximately 10 minutes). The bottleneck reactions of the cycle are the $^{14}\text{O}(e^+ \nu_e)^{14}\text{N}$ and $^{15}\text{O}(e^+ \nu_e)^{15}\text{N}$ beta decays. Therefore, the hot CNO cycle has a temperature-independent rate

$$\dot{n}_{\text{hCNO}} = 4.6 \times 10^{15} \text{ erg g}^{-1} \text{ s}^{-1} X_{\text{CNO}}. \quad (6)$$

Dividing the energy-generation rate by $Q_{\text{hCNO}} = (26.73 - 1.05 - 1.00) \text{ MeV}$, where we consider the average energies of neutrinos for the two decays, 1.05 and 1.00 MeV, respectively, yields

$$\dot{n}_{\text{hCNO}} = 1.16 \times 10^{20} \text{ cm}^{-3} \text{ s}^{-1} \rho X_{\text{CNO}}. \quad (7)$$

Since we do not have the information for all nuclear species relevant for the cold and hot CNO cycles, we do not know the abundance of the bottleneck species, which are ^{14}N for cold, and ^{14}O and ^{15}O for hot CNO cycles, respectively. Therefore, we simply assume that the mass fraction of these species is the same as that of the representative CNO species.

When the hot CNO cycle works in a high-temperature environment, the cold CNO cycle does not work anymore. Because the expression of the cold CNO cycle (Equation (6)) is lower than that of the hot CNO cycle (Equation (5)) when the latter works for the hydrogen burning, to account for the transition from cold to hot CNO cycles, we take the smaller rate for the total process as

$$\dot{n}_{\text{CNO}} = \min(\dot{n}_{\text{cCNO}}, \dot{n}_{\text{hCNO}}). \quad (8)$$

Then, the source terms for the mass fractions of ^1H and ^4He for this process are, respectively,

$$\dot{n}_p|_{\text{CNO}} = -4\dot{n}_{\text{CNO}}, \quad (9)$$

$$\dot{n}_\alpha|_{\text{CNO}} = \dot{n}_{\text{CNO}}. \quad (10)$$

2.2.3. Triple-Alpha Reaction

The energy-generation rate of the triple- α reaction is (e.g., R. Kippenhahn & A. Weigert 1990)

$$\dot{q}_{3\alpha} = 5.1 \times 10^8 \text{ erg g}^{-1} \text{ s}^{-1} \rho^3 X_\alpha^3 T_9^{-3} \exp(-4.4 T_9^{-1}), \quad (11)$$

where X_α is the mass fraction of ^4He . We can derive the number rate of the reaction, $\dot{n}_{3\alpha}$, simply by multiplying ρ and dividing $3m(^4\text{He}) - m(^{12}\text{C}) = 3 \cdot 2.425 \text{ MeV} = 1.166 \times 10^{-5} \text{ erg}$ (no neutrino loss) as

$$\dot{n}_{3\alpha} = 4.37 \times 10^{13} \text{ cm}^{-3} \text{ s}^{-1} \rho^3 X_\alpha^3 T_9^{-3} \exp(-4.4 T_9^{-1}). \quad (12)$$

Using this rate, the source terms for the mass fractions of ^4He and CNO species are written as

$$\dot{n}_\alpha|_{3\alpha} = -3\dot{n}_{3\alpha}, \quad (13)$$

$$\dot{n}_{\text{CNO}}|_{3\alpha} = \dot{n}_{3\alpha}. \quad (14)$$

In summary, the evolution equations of the mass fractions are written as

$$\partial_\mu(\sqrt{-g} \rho X_p u^\mu) = m_u \sqrt{-g} (-4\dot{n}_{\text{CNO}}), \quad (15)$$

$$\partial_\mu(\sqrt{-g} \rho X_\alpha u^\mu) = 4m_u \sqrt{-g} (\dot{n}_{\text{CNO}} - 3\dot{n}_{3\alpha}), \quad (16)$$

$$\partial_\mu(\sqrt{-g} \rho X_{\text{CNO}} u^\mu) = 12m_u \sqrt{-g} \dot{n}_{3\alpha}. \quad (17)$$

The breakout reactions from the CNO cycles and resulting rapid proton capture (rp -) process are not taken into account due to the simple treatment of the nuclear reaction and the limited number of nuclear species considered in this study. Those reactions can be potential sources of additional energy generation in the collapse of supermassive stars (e.g., C. Nagele et al. 2023a; C. Nagele & H. Umeda 2024).

¹⁰ <https://www-nds.iaea.org/public/download-endf/ENDF-B-VIII.0/decay/>

2.3. Equation of State

In the present work, we assume that the matter consists of ions with a mixture of ^1H , ^4He , and CNO species, photons, electrons, and thermally generated electron–positron (e^-e^+) pairs. We further assume that the atoms are fully ionized, because this is a good approximation inside the star, and the photons are thermalized with the same temperature as the ions and electrons. Then, the specific internal energy, ε , is divided into the three components as

$$\varepsilon = \varepsilon_{\text{ion}} + \varepsilon_{\gamma} + \varepsilon_e, \quad (18)$$

where the contribution of the ions, photons, electrons, and positrons can be written, respectively, as

$$\varepsilon_{\text{ion}} = \frac{3}{2} \frac{k_{\text{B}}T}{\langle A \rangle m_{\text{u}}} + \frac{\langle \Delta m \rangle c^2}{m_{\text{u}}}, \quad (19)$$

$$\varepsilon_{\gamma} = \frac{a_{\text{rad}}T^4}{\rho}, \quad (20)$$

$$\varepsilon_e = \frac{e_e(n_e, T)}{\rho}. \quad (21)$$

Here, a_{rad} is the radiation constant, e_e is the internal energy density of electrons (including the rest mass of e^-e^+ pairs), $\langle A \rangle$ is the average mass number of the ions, and $\langle \Delta m \rangle$ is the average mass excess per baryon (which also includes the mass of electrons). The definitions of the latter two are

$$\frac{1}{\langle A \rangle} := \sum_I \frac{X_I}{A_I}, \quad (22)$$

$$\langle \Delta m \rangle := \sum_I (m_I - A_I m_{\text{u}}) \frac{X_I}{A_I} = \sum_I \Delta m_I \frac{X_I}{A_I}, \quad (23)$$

with $\Delta m_I = m_I - A_I m_{\text{u}}$, where m_I is the atomic mass, which contains the mass of electrons $Z_I m_e$. For the CNO species, we assumed $A_{\text{CNO}} = 12$, $Z_{\text{CNO}} = 6$, and $\Delta m_{\text{CNO}} = 0$.

In the same manner, the pressure P is divided into three components as

$$P = P_{\text{ion}} + P_{\gamma} + P_e, \quad (24)$$

where

$$P_{\text{ion}} = \frac{\rho k_{\text{B}}T}{\langle A \rangle m_{\text{u}}}, \quad (25)$$

$$P_{\gamma} = \frac{a_{\text{rad}}T^4}{3}, \quad (26)$$

$$P_e = P_e(n_e, T). \quad (27)$$

The internal energy density and the partial pressure of electrons and thermal e^-e^+ pairs, e_e and P_e , are functions of the net number density of electrons $n_e = n_{e^-} - n_{e^+}$ (n_{e^-} and n_{e^+} are the number densities of electrons and positrons, respectively) and temperature T , and are tabulated using the Timmes equation of state (F. X. Timmes & D. Arnett 1999; F. X. Timmes & F. D. Swesty 2000). The detailed implementation is described in Appendix A. The electron fraction $Y_e = n_e/n_b$ is defined, by using the charge neutrality, as

$$Y_e = \sum_I \frac{Z_I}{A_I} X_I. \quad (28)$$

2.4. Heating by Nuclear Burning

In this subsection, we briefly explain how heating by nuclear burning is incorporated into our relativistic framework. We incorporate the heating without having any direct source terms for the fluid (i.e., Equation (1)). We instead solve the change in the composition as in Section 2.2.1. Below, we will see how this leads to the heating.

For simplicity, we consider the case without the mechanical work. The first law of thermodynamics then reads as

$$\left. \frac{dq}{dt} \right|_{\nu} = \frac{d\varepsilon}{dt} = \frac{d\varepsilon_{\text{int}}}{dt} + \frac{c^2}{m_{\text{u}}} \frac{d\langle \Delta m \rangle}{dt}, \quad (29)$$

where the term on the left-hand side refers to the possible energy change caused by neutrino emission. On the rightmost side, we decompose ε into the components of purely internal (ε_{int} , i.e., all the terms in Equation (18) except for the second term in Equation (19)) and rest-mass (the second term in Equation (19)) origins. Here, d/dt is the time derivative in the fluid rest frame ($=u^{\alpha}\partial_{\alpha}$).

The change in ε_{int} is then described as

$$\frac{d\varepsilon_{\text{int}}}{dt} = \left. \frac{dq}{dt} \right|_{\nu} - \frac{c^2}{m_{\text{u}}} \frac{d\langle \Delta m \rangle}{dt} \quad (30)$$

$$= \left. \frac{dq}{dt} \right|_{\nu} - \frac{c^2}{m_{\text{u}}} \sum_I \frac{\Delta m_I}{A_I} \frac{dX_I}{dt}. \quad (31)$$

The second term, with a negative sign, shows that the heating caused by nuclear burning is a result of the change in the rest mass. For the CNO cycle, $dX_{\alpha}/dt = -dX_p/dt$, and the corresponding change in ε_{int} is

$$\left. \frac{d\varepsilon_{\text{int}}}{dt} \right|_{\text{CNO}} = \left. \frac{dq}{dt} \right|_{\text{CNO}} + \frac{c^2}{4m_{\text{u}}} (4m(^1\text{H}) - m(^4\text{He})) \frac{dX_{\alpha}}{dt}. \quad (32)$$

As mentioned in Section 2.2.1, two neutrinos are emitted in a CNO cycle. We can thus write the neutrino loss term as

$$\left. \frac{dq}{dt} \right|_{\text{CNO}} = -\frac{E_{\nu, \text{CNO}}}{4m_{\text{u}}} \frac{dX_{\alpha}}{dt}, \quad (33)$$

where $E_{\nu, \text{CNO}}$ (≈ 2 MeV for both cold and hot CNO cycles) is the average energy of two neutrinos emitted in a cycle. In total, the change in the internal energy by hydrogen burning via the CNO cycle is written as

$$\left. \frac{d\varepsilon_{\text{int}}}{dt} \right|_{\text{CNO}} = \frac{1}{4m_{\text{u}}} (4m(^1\text{H})c^2 - m(^4\text{He})c^2 - E_{\nu, \text{CNO}}) \frac{dX_{\alpha}}{dt}. \quad (34)$$

If we ignore the neutrino emission, i.e., dropping $E_{\nu, \text{CNO}}$ in the last expression, the energy generation is overestimated by $\approx 2 \text{ MeV}/26.7 \text{ MeV} \approx 7.5\%$.

2.5. Neutrino Transfer

As mentioned in the previous subsection, neutrinos are emitted as a result of hydrogen burning through beta decays. We implement this process to consistently take into account the energy-generation rate. We solve the neutrino transfer

equations with a truncated moment formalism (M. Shibata et al. 2011) in an energy-integrated way (see S. Fujibayashi et al. 2017 for details).

The matter in the present simulations has only a tiny opacity to neutrinos, and thus, the neutrinos propagate essentially freely after being generated (see Appendix C for justification). Therefore, we do not take any absorption and scattering processes into account in the neutrino transfer.

We only consider the electron-type neutrinos emitted from the CNO cycle. In this process, the extracted energy is $E_{\nu, \text{CNO}} \approx 2 \text{ MeV}$ per cycle. Thus, the energy emission rate per unit volume per unit time in the fluid rest frame is $E_{\nu, \text{CNO}} \dot{n}_{\text{CNO}}$, which means that the source terms in Equations (1) and (2) can be written as

$$S^\alpha = E_{\nu, \text{CNO}} \dot{n}_{\text{CNO}} u^\alpha. \quad (35)$$

The thermal production of neutrino–antineutrino pairs by, e.g., the photoneutrino, electron–positron pair annihilation, and plasma neutrino processes (N. Itoh et al. 1996), is a potentially important cooling process for the dynamics of the collapsing supermassive star core. In this work, however, those neutrino emission processes are not considered due to the following reasons: First, as H. Uchida et al. (2017) showed, the central region of the core, in which the thermal production of neutrinos proceeds efficiently, is anyway swallowed into a newly formed black hole in our setup. Thus, the effect of neutrino cooling is dynamically unimportant. Second, in the phase after the black hole formation, the thermal neutrino production timescale is much longer than the dynamical timescale. Therefore, the neutrino cooling process is also unimportant in the later phase (see Section 4.5). We note that the importance of the neutrino cooling depends on the initial setup of the collapse. If the supermassive star core is likely to explode by nuclear burning (e.g., C. Nagele et al. 2020), neglecting the neutrino cooling overestimates the possibility of the explosion and the resulting explosion energy.

2.6. Initial Profiles of Supermassive Stars

As the initial conditions of the simulations, we employ marginally stable general relativistic equilibrium states of supermassive star cores, which are constructed in the same way as in H. Uchida et al. (2017). In the construction, we assume uniform radiation entropy per baryon and uniform composition. This is a good approximation for the supermassive star cores fully mixed by convection. With this assumption, together with the fact that the system is highly radiation pressure dominated, a polytropic equation of state with the polytropic index close to 3 can be used to construct the equilibrium states.

The stability of supermassive star cores against the general relativistic instability is identified in terms of a fitting formula derived in M. Shibata et al. (2016; i.e., Equation (28) of that paper; see also M. Shibata et al. 2025). Although this formula is valid only for rigidly rotating supermassive star cores, we use it for approximately identifying the stability of the differentially rotating case. Our present numerical simulations show that the formula works well for identifying the stability at least for moderately differentially rotating cases with $\hat{A} \geq 1$ (see below).

A word of caution is appropriate here. Supermassive stars in reality are likely to increase their mass with a very high accretion rate $\gtrsim 0.1 M_\odot \text{ yr}^{-1}$ until the onset of the general relativistic instability. As a result, they have a more

massive radiative layer than their nonaccreting counterparts (C. Nagele & H. Umeda 2024). However, the entropy per baryon in an inner radiative layer of supermassive stars increases with radius only gradually (T. Hosokawa et al. 2013; H. Umeda et al. 2016). Therefore, it would be a reasonable approximation to model both the convective core and inner radiative layer as a core of the supermassive star that has an isentropic structure. On the other hand, as a consequence of the rapid accretion, their outer radiative and surface convective layers are likely to form an inflated envelope with a radius $\sim 10^{15} \text{ cm}$, which has much higher entropy per baryon than that in the inner region (T. Hosokawa et al. 2013; H. Umeda et al. 2016; L. Haemmerlé et al. 2018; H. Saio et al. 2024). Thus, we focus only on the convective core and inner radiative layer of accreting supermassive stars, which contain 80%–90% of the entire stellar mass (see Figure 2 of T. Hosokawa et al. 2013). As the envelope is very dilute, it is not likely that the neglected outer region has a significant effect on the core collapse and subsequent black hole plus torus formation. Nevertheless, the presence of the envelope can have an influence on the stability of the whole supermassive star if the envelope mass is not negligible (e.g., C. Nagele et al. 2022; H. Saio et al. 2024 for the stability analysis of realistic structures of supermassive stars).

The initial data are listed in Table 1. For the “H”-series, we assume that the general relativistic instability sets in during the early hydrogen-burning phase, and thus, the stellar composition is assumed to be primordial with $X_p = 0.75$ and $X_\alpha = 0.25$ together with a low metallicity of $X_C = 5 \times 10^{-9}$ (J. R. Bond et al. 1984). Assuming that the energy-generation rate is equal to the Eddington luminosity, we find the central temperature as $T_c \approx 1.5 \times 10^8 \text{ K}$. For the “He”-series, on the other hand, we assume that the instability sets in at the beginning of the helium-burning phase, and thus, we initialize the star with $X_\alpha = 1$ and $T_c \approx 3 \times 10^8 \text{ K}$. We note that the models H1, He1, H4, and He4 are essentially the same as models A1, A2, A3, and A4 in H. Uchida et al. (2017).

For most of the models, we assume rigid rotation for the angular velocity. The H4 and He4 models are at the mass-shedding limit, i.e., the rotation velocity at the surface of the core in the equatorial plane is that of a Keplerian orbit. The other rigid rotation models (H1–H3 and He1–He3) have a smaller surface velocity (see the column of $T_{\text{kin}}/|W|$ of Table 1, which indicates how fast the star rotates). Here, the kinetic energy and proper mass of the system are defined by

$$T_{\text{kin}} = \int \rho u^t \sqrt{-g} (1 + \langle \Delta m \rangle / m_u) \frac{1}{2} (w^2 - 1) d^3x, \quad (36)$$

$$M_p = \int \rho u^t \sqrt{-g} (1 + \varepsilon / c^2) d^3x, \quad (37)$$

where the factor $(1 + \langle \Delta m \rangle / m_u)$ in Equation (36) corrects the difference of the mass per baryon from m_u . We then define the gravitational potential energy of the system as $W = M_0 c^2 - M_p c^2 - T_{\text{kin}}$, where M_0 is the gravitational (Arnowitt–Deser–Misner; ADM) mass of the system (R. Arnowitt et al. 1960). To explore the effect of more rapid rotations, we prepare “Hdif”-series, for which we assume a differential rotation using the so-called j -constant law with varying the degree of differential rotation as $\hat{A} = 1$ –2 (T. W. Baumgarte et al. 2000; see Table 1 for the value of \hat{A}). Note that $\hat{A} \rightarrow \infty$ corresponds to the rigidly rotating configuration. For these

Table 1
List of Initial Data and Their Key Properties

Model	M_0 (M_\odot)	R_{c0} (cm)	$T_{\text{kin}}/ W $	$\alpha_{c,0}$	$\gamma_{c,0} - 4/3$	\hat{A}	s/k_B	$\rho_{c,0}$ (g cm^{-3})
H1	2.1×10^5	1.7×10^{13}	0.002	0.992	0.0026	∞	450	1.12
H2	3.2×10^5	2.3×10^{13}	0.004	0.990	0.0021	∞	550	0.82
H3	4.3×10^5	2.7×10^{13}	0.006	0.988	0.0018	∞	630	0.80
H4	6.9×10^5	4.4×10^{13}	0.009	0.985	0.0014	∞	800	0.61
Hdif1	9.2×10^5	5.0×10^{13}	0.011	0.983	0.0012	2	920	0.53
Hdif2	1.1×10^6	5.3×10^{13}	0.013	0.981	0.0012	1.5	1000	0.53
Hdif3	1.9×10^6	7.4×10^{13}	0.018	0.976	0.0009	1.0	1300	0.33
He1	5.0×10^4	4.3×10^{12}	0.002	0.992	0.0023	∞	210	17.8
He2	7.1×10^4	5.1×10^{12}	0.004	0.990	0.0019	∞	250	16.3
He3	9.6×10^4	6.1×10^{12}	0.006	0.988	0.0016	∞	300	15.6
He4	1.6×10^5	1.0×10^{13}	0.009	0.985	0.0013	∞	380	11.3

Note. From left to right, the model name, gravitational mass, equatorial radius, the ratio of kinetic to gravitational potential energy, central lapse, central adiabatic index minus 4/3, the parameter that indicates the degree of differential rotation \hat{A} , central entropy per baryon, and central rest-mass density. Note that the total baryon rest mass is approximately equal to the gravitational mass.

models, the axial ratio (polar radius to equatorial radius) is set to be the same as that of H4, which is $\approx 2/3$.

In Table 1, we find that the central adiabatic index is closer to 4/3 and that the central lapse is smaller for supermassive star cores with higher values of $T_{\text{kin}}/|W|$. This indicates that the rotation stabilizes the supermassive star cores against the general relativistic instability, and hence, the rotating stars have to be more compact and radiation dominated to become unstable (details are discussed in our accompanying paper; M. Shibata et al. 2025).

The mass of the marginally stable supermassive star cores that are studied in this paper is in the range between $\approx 2 \times 10^5$ and $\approx 2 \times 10^6 M_\odot$ for the hydrogen-burning models and between $\approx 5 \times 10^4$ and $\approx 2 \times 10^5 M_\odot$ for the helium-burning models. For a given value of $T_{\text{kin}}/|W|$, the mass of the marginally stable supermassive star becomes smaller for a more evolved one. For example, for an evolved supermassive star core in the helium-burning phase, the fractions of carbon and oxygen increase. For such a supermassive star, the threshold mass for the collapse associated with the general relativistic instability is by a factor of 2–3 lower than $5 \times 10^4 M_\odot$ (M. Shibata et al. 2025). In this paper, we do not pay attention to such relatively low-mass supermassive star cores but only to high-mass ones. In the follow-up work, we plan to explore the fate of the collapse of the low-mass supermassive star cores.

2.7. Grid Setup

Following our previous works (e.g., S. Fujibayashi et al. 2020a, 2020b, 2020c), we employ cylindrical coordinates denoted by (x, z) with mirror symmetry with respect to the $z = 0$ plane. For both directions, the grid is assigned in the following manner: $x_i = x_{i-1} + dx_i$ with the innermost grid located at $x_0 = 0$ and $dx_i = dx_0$ for $x_{i-1} < r_{\text{uniform}}$. Otherwise, $dx_i = dx_{i-1}(1 + \eta)$ with a small number $\eta > 0$. Here, $i = 0-N$ with N denoting the grid size.

In this work, the grid spacing is determined so that the number of grid points for a large radius is suppressed while keeping enough angular resolution in that region. For a given innermost grid spacing dx_0 , the size of the uniform-grid region r_{uniform} , the location of the outer boundary $L = x_{N-1/2} := (x_{N-1} + x_N)/2$ ($i = N$ corresponds to the first ghost cell), and the approximate angular resolution $dx_{N-1}/x_{N-1/2}$, we

determine N and η . In this study, we always take $L = 1800 r_g$, $r_{\text{uniform}} = r_g$, and $dx_{N-1}/L = (\pi/2)/96$, where $r_g = GM_0/c^2$.

2.8. Regridding

The collapsing supermassive stars are becoming more and more compact with time, and thus, a grid that resolves the curvature scale of the collapsing matter at each moment is required. In addition, to numerically evolve the formed black hole accurately, a sufficient grid resolution with $dx_0 \ll r_g$ is necessary, although we need such high grid resolutions only after a black hole is formed. To save computational resources, thus, we employ a *regridding* algorithm (e.g., M. Shibata & S. L. Shapiro 2002) in this work.

For the first run of each simulation, we take $dx_0 = 0.5r_g$ and decrease it successively during the collapse. For each run with a given value of dx_0 , we determine the time of regridding using the central lapse α_c , because it indicates the effective compactness of the star, $GM/c^2R \sim 1 - \alpha_c$. When $1 - \alpha_c$ of a run becomes half of that at its start time, we stop the run and restart the simulation with finer grid resolutions. We set a new value of dx_0 , which is typically half of that in the previous run. As dx_0 decreases, the total number of grid points and the parameter η are set to keep the same values of L and dx_{N-1}/L . By doing this, the collapsing stellar radius is always resolved with a similar number of grids.

In the regridding process, we map the quantities to be evolved onto the new, finer grid points with a third-order Lagrange interpolation scheme. At the beginning of each run, assuming a conformally flat space, the constraint equations of general relativity are solved to obtain the initial condition for the metric variables based on a predetermined energy-momentum distribution. We note that assuming the spatial conformal flatness is a good approximation because the maximum nondiagonal component of the spatial metric $\hat{\gamma}_{ij}$ is always in the order of 10^{-4} when the criterion of the regridding is satisfied. In other words, the regridding has to be performed for the case that the collapsing star is not very compact. In the present work, the final regridding is performed when $\alpha_c = 0.85$. For the final run, we choose $dx_0 = 0.04r_g$ and $0.025r_g$ for standard- and high-resolution runs, respectively (they are labeled with the letters ‘‘L’’ and ‘‘H,’’ respectively).

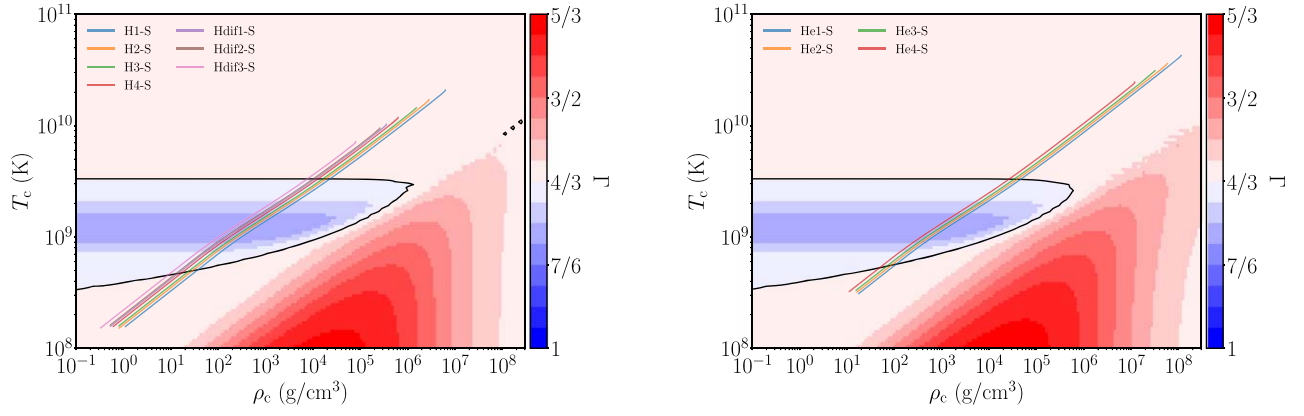


Figure 1. Evolution of the central density and central temperature of supermassive star cores up to the black hole formation (solid curves). The adiabatic index is shown in color. The black curves denote the contour of $\Gamma = 4/3$.

The coordinate parameters for the first run are calculated as $(N, \eta) = (252, 0.01668)$. After the final regridding, on the other hand, they are $(N, \eta) = (424, 0.01682)$ and $(488, 0.01693)$ for standard- and high-resolution runs, respectively.

2.9. Ejecta Diagnostics

We define the unbound matter (ejecta) as the component that has a positive value of the specific binding energy as

$$e_{\text{bind}} = \frac{-T_{(\text{n})}{}^t{}_t}{\rho u^t} - (c^2 + \varepsilon_{\text{min}}). \quad (38)$$

This is conserved along flow lines in stationary spacetime (H. Uchida et al. 2017; S. Fujibayashi et al. 2021). Here, $T_{(\text{n})}{}^{\mu\nu}$ is again the energy-momentum tensor of the fluid, and $\varepsilon_{\text{min}} := \langle \Delta m \rangle c^2 / m_{\text{u}}$ is the minimum specific internal energy. In this study, we evolve the composition dynamically. Thus, ε_{min} is defined more precisely than those defined using an equation of state for which nuclear statistical equilibrium is assumed in their construction.

With the definition of the specific binding energy by Equation (38), the mass and asymptotic kinetic energy of the ejecta at a given time are, respectively, defined as

$$M_{\text{ej}} = \int \rho u^t \sqrt{-g} \Theta(e_{\text{bind}}) d^3x + \int^t \int \rho u^k \sqrt{-g} \Theta(e_{\text{bind}}) ds_k dt, \quad (39)$$

$$K_{\text{ej}} = \int e_{\text{bind}} \rho u^t \sqrt{-g} \Theta(e_{\text{bind}}) d^3x + \int^t \int f_{\text{bind}}^k \sqrt{-g} \Theta(e_{\text{bind}}) ds_k dt, \quad (40)$$

where the first and second terms in each expression are the contributions of the matter located inside the computational domain and that flown out from the domain. ds_k is the area element at the outer boundary of the computational domain, Θ is the Heaviside function, and

$$f_{\text{bind}}^k = -T_{(\text{n})}{}^k{}_t - (c^2 + \varepsilon_{\text{min}}) \rho u^k \quad (41)$$

is the flux density associated with the energy density. The average asymptotic velocity of the ejecta is then defined by

$$V_{\infty}/c = \sqrt{1 - \Gamma_{\infty}^{-2}} \quad (42)$$

with the average asymptotic Lorentz factor

$$\Gamma_{\infty} = 1 + K_{\text{ej}}/M_{\text{ej}}c^2. \quad (43)$$

3. Results

3.1. Evolution Outline

For all the models, effects of nuclear burning play only a minor role during the collapse, and as a result, the collapse proceeds monotonically until a black hole is formed in a dynamical timescale. This result is consistent with the previous findings by H. Uchida et al. (2017).

Figure 1 displays the evolutionary paths of the central density and central temperature until the formation of the black hole in the ρ - T plane with the adiabatic index shown in color. For all the models, the initial position of the central density and central temperature (left bottom edge of each line; see also Table 1) lies outside the domain for the pair-production instability, i.e., $\gamma_c > 4/3$. This indicates that the collapses are triggered by the general relativistic instability.

In the early phase of the collapse, the density and temperature increase approximately adiabatically, i.e., $T \propto \rho^{1/3}$. After the evolutionary path goes through the pair-unstable region, the temperature gradient with respect to the density, $dT/d\rho$, becomes slightly shallower; a part of the internal energy gained by the compression is converted to the rest-mass energy of e^-e^+ pairs. The path goes outside of the pair-unstable region eventually for $T \gtrsim 3 \times 10^9$ K, but the collapse proceeds farther without bounce in our models, and finally, a black hole is formed.

The top panels of Figure 2 show the time evolution of the black hole mass estimated from the equatorial circumference length of the apparent horizon C_c (e.g., M. Shibata 2016),

$$M_{\text{BH}} = \frac{c^2 C_c}{G 4\pi}, \quad (44)$$

normalized by the initial ADM mass of the system. It shows that over 90% of the stellar matter in the mass becomes a black hole. The fraction is smaller for the higher $T_{\text{kin}}/|W|$ cases because a greater fraction goes into a torus formed. The bottom panels show the dimensionless spin χ of the formed black hole. Assuming the relations for Kerr black holes, it is determined

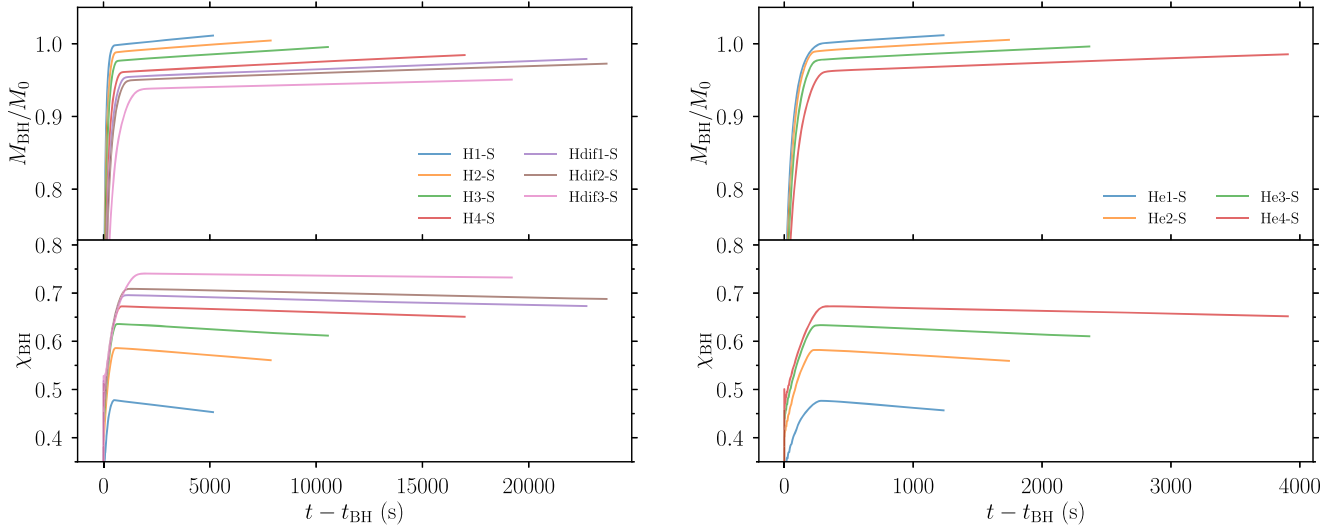


Figure 2. Time evolution of the black hole mass and dimensionless spin for all the models with standard grid resolutions studied in this paper.

by solving

$$\frac{C_p}{C_e} = \frac{\sqrt{2\hat{r}_+(\chi)}}{\pi} \int_0^{\pi/2} \left(1 - \frac{\chi^2}{2\hat{r}_+(\chi)} \sin^2 \theta\right)^{1/2} d\theta \quad (45)$$

for χ (e.g., K. Kiuchi et al. 2009). Here, C_p is the polar circumference length of the apparent horizon, and $\hat{r}_+(\chi) = 1 + \sqrt{1 - \chi^2}$ is the event-horizon radius normalized by GM_{BH}/c^2 . The dimensionless spins of the formed black holes are found to span from ≈ 0.45 to ≈ 0.75 depending on the initial values of $T_{\text{kin}}/|W|$.

The matter with a sufficiently high angular momentum, which is located at a large cylindrical radius initially, forms a centrifugally supported torus around the black hole. The torus formation starts at $t - t_{\text{BH}} = 1000\text{--}2000$ s (t_{BH} is the time when the BH forms) for H-series and $200\text{--}300$ s for He-series. After the formation of the torus, the mass infall to the black hole is suppressed: The mass and dimensionless spin of the black hole saturate at the torus formation. The slow changes in the black hole mass and dimensionless spin after the saturation are caused mostly by numerical artifacts (see Section 3.4).

The collapse triggered by the general relativistic instability proceeds rather coherently. In addition, there is no efficient cooling mechanism (the process is approximately adiabatic; see Section 4.5). As a result, the torus experiences a strong bounce soon after its formation due to the centrifugal barrier. The shock wave formed by the bounce drives the mass ejection (see W. H. Lee & E. Ramirez-Ruiz 2006; Y. T. Liu et al. 2007; H. Uchida et al. 2017 for a detailed description of the ejecta formation process). After that, the torus relaxes to a quasi-stationary state around the black hole in the simulations that do not take into account viscous effects (see Figure 6).

3.2. Properties of Torus-shock-induced Ejecta

Figure 3 shows the evolution of the mass, kinetic energy, and average velocity of the ejecta generated by a shock formed at the inner surface of the torus for the H series (left) and He series (right). The ejecta mass of each model is normalized by the initial gravitational mass of the system (note that the relative difference between the gravitational mass and baryon rest mass is only $\sim 10^{-5}$). For each curve, the time origin is

shifted by the black hole formation time, t_{BH} . As found in H. Uchida et al. (2017), M_{ej}/M_0 increases with the increase of $T_{\text{kin}}/|W|$ for relatively low values of $T_{\text{kin}}/|W|$. However, the ejecta mass fraction saturates at $T_{\text{kin}}/|W| \sim 0.01$ as $M_{\text{ej}}/M_0 \sim 0.01$. This saturation level is similar for the differentially rotating cases (Hdif-series) and the more compact He models (see Table 2).

Figure 4 shows the relation between the kinetic energy and mass of the bounce-shock-driven ejecta for all the models studied in this paper. We find that the kinetic energy of the ejecta is approximately proportional to the ejecta mass, in particular for rapidly rotating models. This is reflected in the result that the average velocity of the ejecta is universal among the models as $\sim 0.2c$ (see the gray line in Figure 4). This universally high velocity indicates that the mass ejection is driven in the vicinity of the black hole with the typical radius of $\sim 10\text{--}20r_g$.

For a variety of models, the kinetic energy of the ejecta exceeds 10^{55} erg. Supermassive stars are believed to be formed in the center of protogalaxies, likely surrounded by an accreting dense gas cloud. The large kinetic energy of the ejecta is likely to be injected into such a cloud, being dissipated and possibly leading to subsequent electromagnetic radiation. This process is similar to the stage prior to the shock breakout of a supernova explosion in a massive star. The cloud is swept by the ejecta originating from the supermassive star, becoming a part of the ejecta. Since the kinetic energy and mass of the total ejecta are much larger than those of massive stars, the luminosity and duration for the subsequent radiation can be much larger than the typical supernovae (e.g., H. Uchida et al. 2017). This point will be discussed in Section 4.

Figure 5 shows the spatial distribution of the rest-mass density and terminal velocity at $t - t_{\text{BH}} \approx 6900$ s for model H4-H. The terminal velocity for unbound ($e_{\text{bind}} > 0$) matter is locally defined as

$$[1 - (v_{\infty}/c)^2]^{-1} = 1 + e_{\text{bind}}/c^2. \quad (46)$$

Note that this definition is conceptually the same as the average velocity in Equation (42), as the positive total energy of the ejecta is assumed to asymptotically be the kinetic energy (see Equation (40)). The outer edge of the ejecta is found to have $v_{\infty}/c \lesssim 1$. This shows that a fraction of the ejecta component is

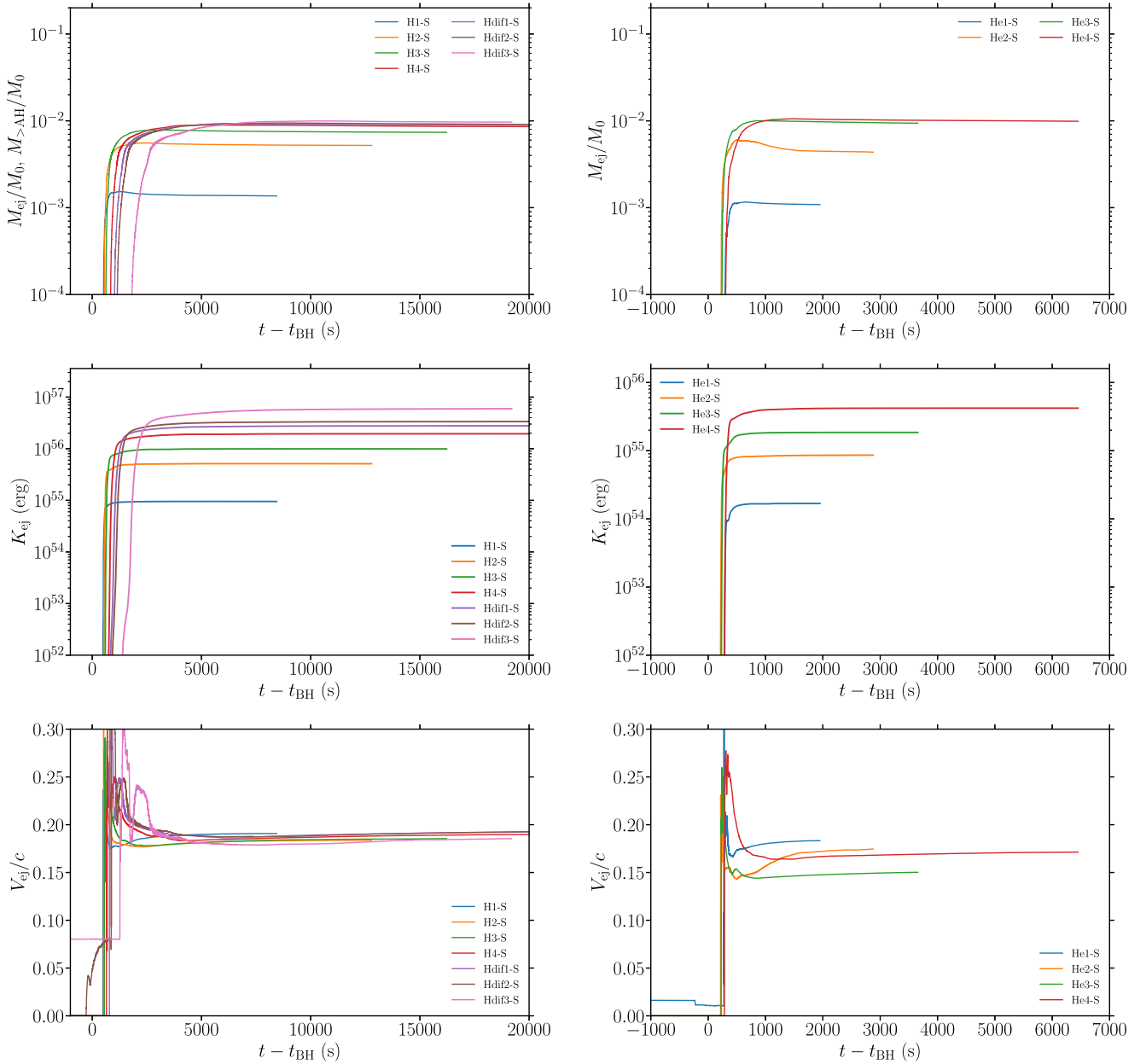


Figure 3. Time evolution of the mass (top panels), asymptotic kinetic energy (middle), and average asymptotic velocity (bottom) of the ejecta. The left and right panels are the results of H- and He-series, respectively.

accelerated to such a high velocity at the stellar surface, which has a steep density gradient (e.g., E. Waxman & D. Shvarts 1993).

It is also found that the ejecta has a quasi-spherical shape, although the bounce of the torus drives mass ejection toward the polar direction (H. Uchida et al. 2017). After breaking out from the stellar surface, the ejecta expands laterally to become a quasi-spherical geometry. In addition, the shock wave associated with the bounce is diffracted in the stellar envelope toward the equatorial direction, and then, an outer part of the stellar envelope becomes unbound by being swept up by the shock wave. This effect also contributes to developing the quasi-spherical ejecta.

The nuclear composition of the ejecta is essentially the same as that in the initial condition because the matter in which nuclear burning proceeds efficiently is swallowed by the newly

formed black hole. In addition, the density and temperature of the ejecta are too low for efficient nuclear reactions: Figure 6 shows the radial profiles of the rest-mass density and temperature along x - and z -axes for model H4-H. The density and temperature of the ejecta are, at highest, $\rho \sim 10 \text{ g cm}^{-3}$ and $T \approx 5 \times 10^8 \text{ K}$ at the time of the shock formation (at $t - t_{\text{BH}} \approx 1000 \text{ s}$). At such a density and temperature, the timescales of the (hot) CNO cycle and triple- α reactions, defined by n_b/\dot{n}_{CNO} and $n_b/\dot{n}_{3\alpha}$, are on order of 10^{12} s at shortest. This timescale is much longer than the dynamical (expansion) timescale of the ejecta. Thus, the nuclear burning does not significantly proceed inside the torus and ejecta. For the primordial initial composition models of H-series, the dominant heavy species in the ejecta will be nitrogen because the ejecta matter does not experience the hot CNO hydrogen burning. Thus, we can assume that the mass of ejected nitrogen

Table 2
Key Results

Model	M_{ej} (M_{\odot})	(M_{ej}/M_0) (%)	K_{ej} (erg)	(K_{ej}/M_0c^2) (%)	V_{ej} (c)	M_{BH} (M_{\odot})	χ_{BH}
H1-S	2.8×10^2	(0.14)	9.5×10^{54}	(0.003)	0.19	2.09×10^5	0.47
H2-S	1.7×10^3	(0.52)	5.1×10^{55}	(0.009)	0.18	3.17×10^5	0.58
H3-S	3.1×10^3	(0.74)	9.9×10^{55}	(0.013)	0.19	4.20×10^5	0.63
H4-S	5.8×10^3	(0.85)	1.9×10^{56}	(0.016)	0.19	6.66×10^5	0.67
Hdif1-S	8.1×10^3	(0.88)	2.8×10^{56}	(0.017)	0.19	8.84×10^5	0.69
Hdif2-S	9.8×10^3	(0.90)	3.4×10^{56}	(0.017)	0.19	1.04×10^6	0.71
Hdif3-S	1.9×10^4	(0.97)	5.9×10^{56}	(0.017)	0.19	1.85×10^6	0.74
He1-S	5.5×10^1	(0.11)	1.7×10^{54}	(0.002)	0.18	5.00×10^4	0.47
He2-S	3.1×10^2	(0.44)	8.6×10^{54}	(0.007)	0.17	7.02×10^4	0.58
He3-S	9.0×10^2	(0.94)	1.9×10^{55}	(0.011)	0.15	9.42×10^4	0.63
He4-S	1.6×10^3	(0.99)	4.2×10^{55}	(0.015)	0.17	1.53×10^5	0.67
H4-v0.03M	5.9×10^3	(0.86)	1.9×10^{56}	(0.016)	0.19
H4-v0.10M	1.0×10^4	(1.46)	2.1×10^{56}	(0.017)	0.15
H4-v0.03SS	7.8×10^3	(1.13)	2.0×10^{56}	(0.016)	0.17
H4-v0.10SS	1.3×10^4	(1.86)	2.2×10^{56}	(0.018)	0.14
H1-H	3.0×10^2	(0.14)	9.9×10^{54}	(0.003)	0.19	2.08×10^5	0.48
H4-H	6.0×10^3	(0.87)	2.0×10^{56}	(0.017)	0.19	6.58×10^5	0.68
He1-H	4.9×10^1	(0.10)	1.5×10^{54}	(0.002)	0.18	4.98×10^4	0.48
He4-H	1.6×10^3	(1.02)	4.4×10^{55}	(0.016)	0.17	1.51×10^5	0.68

Note. From left to right, the model name, ejecta mass, asymptotic kinetic energy and average velocity of the ejecta, mass and dimensionless spin of the formed black hole. In the third and fifth columns, the ratios of the ejecta mass to total mass and ejecta kinetic energy to total mass–energy are also shown in the parentheses. The mass and dimensionless spin of the black hole are measured at $t - t_{\text{BH}} = 1000GM_0/c^3$ for each simulation. The black hole mass and dimensionless spin remain blank for the viscous models: see those for H4-S.

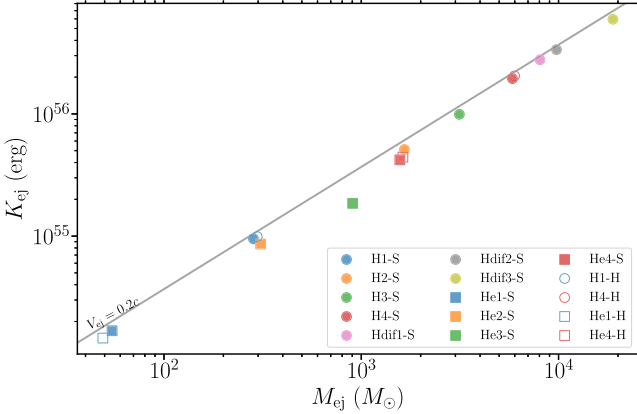


Figure 4. Correlation between the mass and kinetic energy of the ejecta driven by the shock formed in the bounce of the torus. The circle and square markers denote the results of H- and He-series, respectively, while the filled and open markers denote the standard- and high-resolution models, respectively. The gray line denotes the relation assuming a constant ejecta velocity of 0.2c.

for these models is 5×10^{-9} times the ejecta mass in the present study, reflecting the initial composition of the star.

Figure 6 also shows that a stationary torus is developed on the equatorial plane in a timescale of $\sim 10^3$ s. On the other hand, along the symmetric axis (z -axis), the density and temperature decrease gradually due to the mass accretion onto the central black hole. We note that the black hole apparent horizon is located at the radius $\approx 6 \times 10^{10}$ cm for model H4-H at the times shown in Figures 5–7.

3.3. Viscous Evolution of Torus

The torus formed around the black hole may evolve with magnetohydrodynamical processes through the magnetorotational

instability (S. A. Balbus & J. F. Hawley 1991, 1998) in the presence of a seed magnetic field in the supermassive stars. The magnetorotational instability in the torus will develop a turbulent state, which then induces an effective viscosity and drives angular momentum transport and viscous heating. Because no efficient cooling mechanism is present in the present case, a part of the torus matter can become ejecta in the presence of the viscous effects (e.g., S. Fujibayashi et al. 2020a). To investigate the possible outcomes of the viscous evolution, we perform several viscous hydrodynamics simulations with the formalism used in M. Shibata et al. (2017). To assess the largest possible impact, we pick up the postcollapse data for the H4 model as the initial condition of the viscous hydrodynamics. We switch on the viscosity at $t - t_{\text{BH}} \approx 3.4 \times 10^4$ s at which the torus settles down to a stationary state as illustrated in Figure 6. At this time, the bounce-driven shock-heated ejecta is located far from the central domain.

We consider a Shakura–Sunyaev-type kinetic viscous coefficient (N. I. Shakura & R. A. Sunyaev 1973) as

$$\nu = \alpha_{\text{vis}} c_s \ell_{\text{tur}}, \quad (47)$$

where c_s is the sound speed, and α_{vis} is a constant that controls the magnitude of the coefficient. We consider two prescriptions for the length scale of the turbulence ℓ_{tur} . In the first one, we assume a constant value $\ell_{\text{tur}} = 2GM_0/c^2$ as in S. Fujibayashi et al. (2020a). The model with this prescription is denoted by a letter “M” in its name. Since most of the stellar matter collapses into the black hole, the mass of the formed black hole can be approximated by M_0 . Therefore, ℓ_{tur} is approximately the size of the black hole horizon. In the second prescription, we assume

$$\ell_{\text{tur}} = c_s / \Omega_K \quad (48)$$

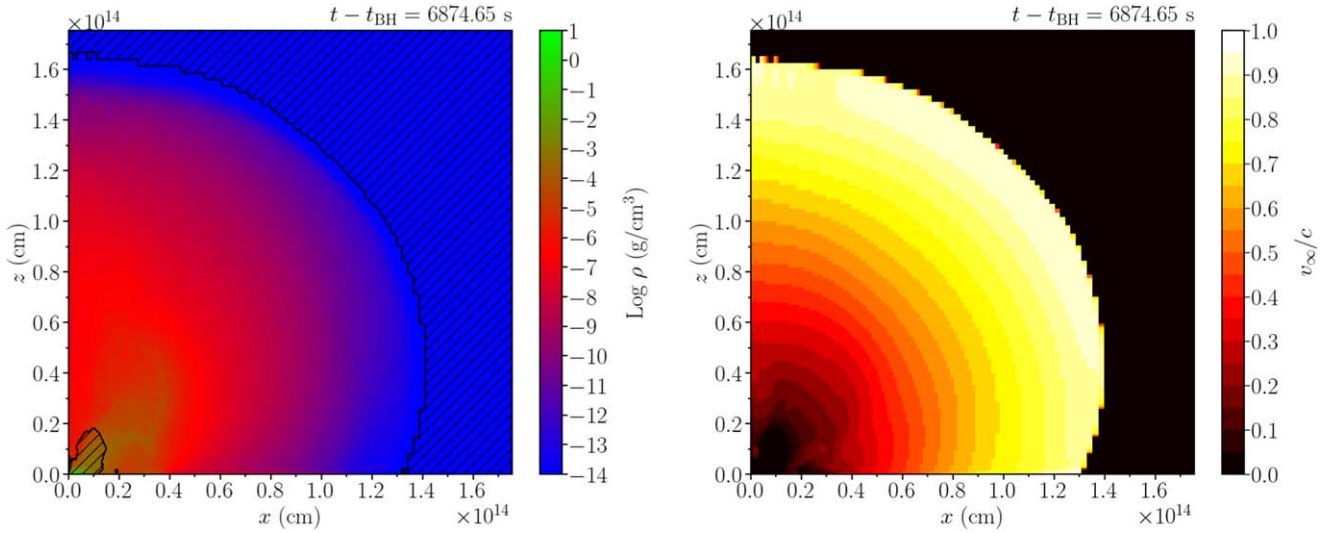


Figure 5. Density (left) and terminal velocity (right) distribution for model H4-H at $t - t_{\text{BH}} \approx 7 \times 10^3$ s. In the left panel, the domain with bound matter is marked by hatched areas.

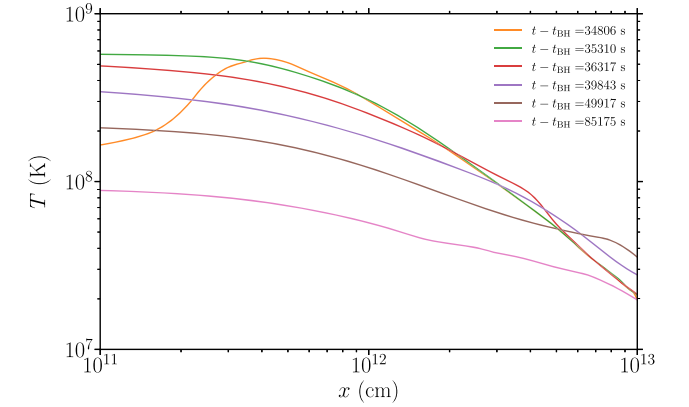
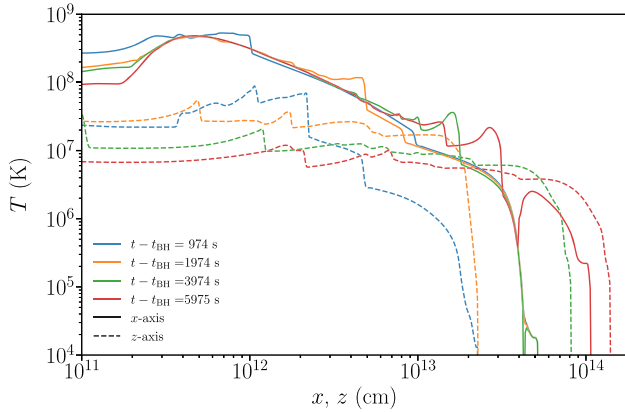
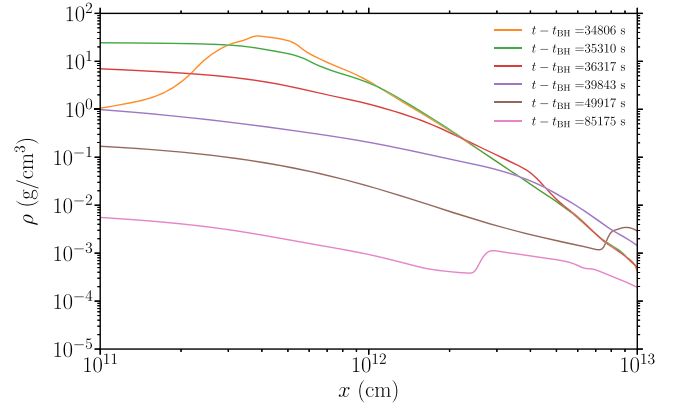
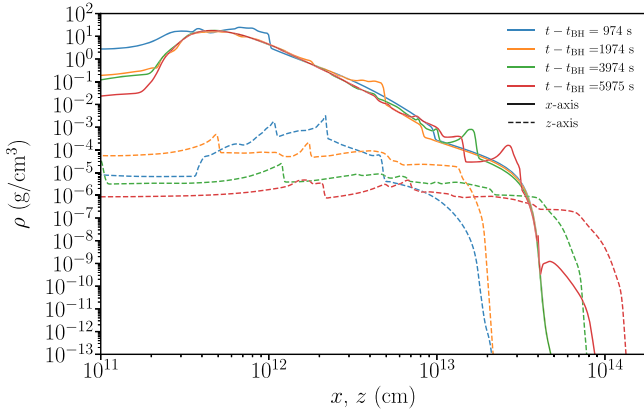


Figure 6. Distribution of density (upper panel) and temperature (lower panel) along the x - and z -axes for model H4-H, especially focusing on the times at which the ejecta is developed.

with the local Keplerian angular velocity Ω_{K} , which is approximated with the derivative of the lapse function as

$$\Omega_{\text{K}} = \sqrt{\frac{c^2}{x} \frac{\partial \alpha}{\partial x}}. \quad (49)$$

The model with this prescription is denoted by “SS.” For a given cell, we use Ω_{K} evaluated on the equatorial plane at the

Figure 7. Density and temperature distribution along the x -axis for model H4-v0.10SS, after switching on the viscosity (at $t - t_{\text{BH}} = 3.4 \times 10^4$ s).

same cylindrical radius. In the far region from the black hole, we have $\alpha \approx 1 - GM_{\text{BH}}/(xc^2)$ along the equatorial direction. Thus, Ω_{K} is reduced to the usual Newtonian expression $\sqrt{GM_{\text{BH}}/x^3}$.

For each viscous prescription, we suppress the viscous coefficient in low-density regions by a factor $(1 - e^{-\rho/\rho_{\text{crit}}})$ with $\rho_{\text{crit}} = 10^{-3} \text{ g cm}^{-3}$ in order not to affect the dynamics of the infalling stellar envelope and expanding ejecta, for which a high effective viscosity is not likely to be induced. For each

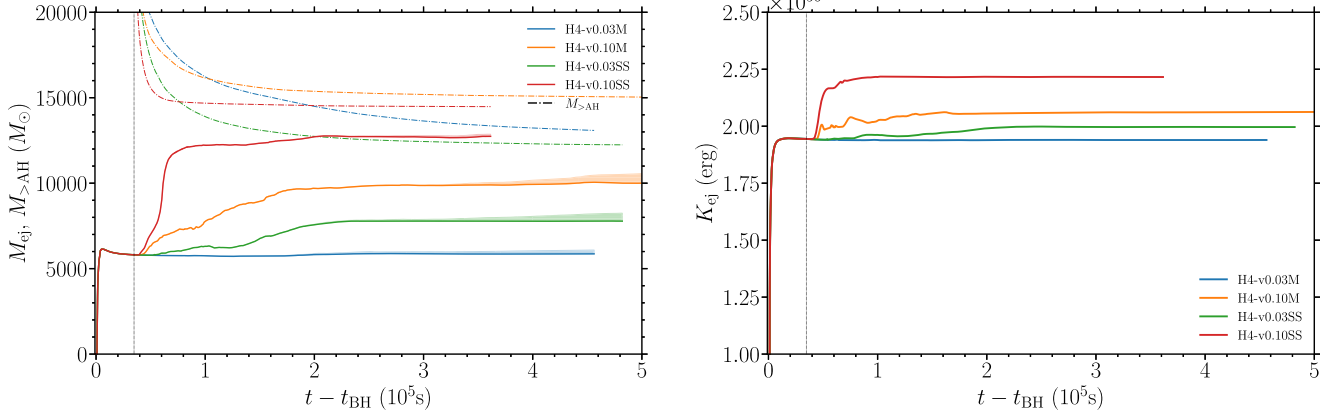


Figure 8. Mass (left) and asymptotic kinetic energy (right) of the total ejecta focusing on the development of the viscosity-driven ejecta. For each panel, the dashed vertical lines at $t - t_{\text{BH}} \approx 3.4 \times 10^4$ s mark the time at which the viscosity is switched on. In the left panel, the shaded bands denote the possible range of the ejecta, considering the still-bound matter that has already escaped from the computational domain. The dashed curves in the left panel show the mass of the matter located outside the apparent horizon $M_{>\text{AH}}$.

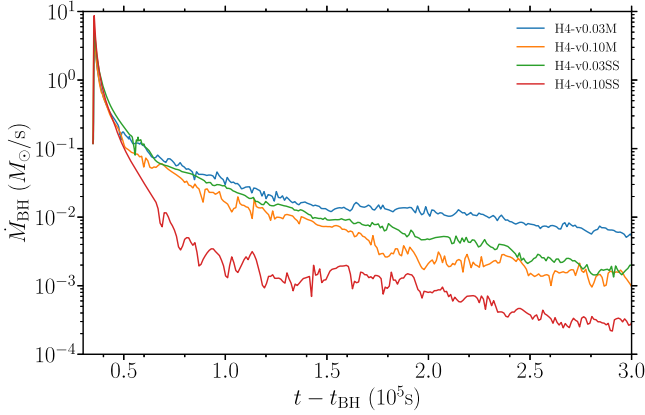


Figure 9. Mass accretion rate onto the black hole for the viscous models after switching on the viscosity. See Section 3.3 for the definition.

prescription of ℓ_{tur} , we use $\alpha_{\text{vis}} = 0.03$ and 0.1 . In the model name, the imposed values of α_{vis} are denoted by the number before the letter denoting the viscosity prescription (e.g., 0.10SS and 0.03M).

Figure 7 shows the radial profiles of density and temperature along the x -axis for different times. After the viscosity is switched on, the density in the inner region of the torus decreases due to the mass accretion onto the black hole and to outward expansion resulting from the angular momentum transport. Also, the temperature decreases accordingly. Thus, the timescale of the nuclear reactions (in this work, CNO cycle and triple- α reaction) becomes longer in the later phase of the torus evolution. We also find that, at the typical torus radius $x \sim 10^{12}$ cm, the viscous timescale is $x^2/\nu \sim 10^4$ s, which is much shorter than the nuclear reaction timescale $\sim 10^{12}$ s at shortest. This implies that the torus matter is accreted onto the central black hole before it is burnt, and therefore, the nuclear burning in the accreting torus has a negligible effect on its evolution.

Figure 8 compares the ejecta properties with different viscous parameters and prescriptions for the viscous H4 models. Here, we note that the viscosity is switched on at $t - t_{\text{BH}} \approx 3.4 \times 10^4$ s. We find that an amount of mass that escapes from the computational domain is still bound according to the criterion based on e_{bind} (see Equation (38)). Such a component may become unbound eventually by being pushed

up by the outflow from the torus launched later. The possible range of the ejecta mass taking such a component into account is also indicated by shading in the same figure. For model H4-v0.10SS, the ejecta mass begins to increase at $t - t_{\text{BH}} \approx 4 \times 10^4$ s with an approximate saturation at $t - t_{\text{BH}} \sim 1 \times 10^5$ s. The ejecta mass increases in this period by $\approx 6.5 \times 10^3 M_{\odot}$. In the same period, the asymptotic kinetic energy of the ejecta increases by $\sim 3 \times 10^{55}$ erg. This indicates that the viscosity-driven ejecta has an average velocity of $\approx 0.07c$. Considering that the remaining bound mass outside the black hole is $\approx 3 \times 10^3 M_{\odot}$ at $t - t_{\text{BH}} = 1 \times 10^5$ s, the viscosity-driven ejecta contributes to the kinetic energy by $\lesssim 5 \times 10^{55}$ erg, which is smaller than that of the torus-shock-driven ejecta ($\approx 2 \times 10^{56}$ erg). The contribution of the viscosity-driven ejecta is even smaller for the models with the other prescription of the turbulence length scale or with the smaller viscous parameter. Thus, the viscosity-driven ejecta is a subdominant component of the entire ejecta in this problem.

Figure 9 shows the mass accretion rate onto the black hole for the four viscous models. The accretion rate is defined by

$$\dot{M}_{\text{BH}} = \int_{\text{AH}} \rho u^k \sqrt{-g} ds_k, \quad (50)$$

where ds_k is the area element on the surface of the apparent horizon. The accretion rate decreases with time after an initial steep rise when the viscosity is switched on. The accreted mass amounts to $\approx 1.3 \times 10^4 - 1.8 \times 10^4 M_{\odot}$, which is accreted mainly in the first $3 \times 10^3 - 1 \times 10^4$ s depending on the adopted viscosity prescriptions and the values of the viscous parameter. For a given value of the viscous parameter, the prescription in Equation (47) leads to a shorter accretion timescale because Equation (47) leads to a longer turbulence length scale than $2GM_0/c^2$, and the larger viscous parameter leads to a shorter mass accretion timescale for a given prescription of the viscosity.

The mass accretion of the black hole could potentially drive a relativistic jet in the presence of magnetic fields and impact energetic transients. This topic will be discussed in Section 4.2.

3.4. Resolution Study

For models H1, H4, He1, and He4, we performed simulations with a higher grid resolution after the last

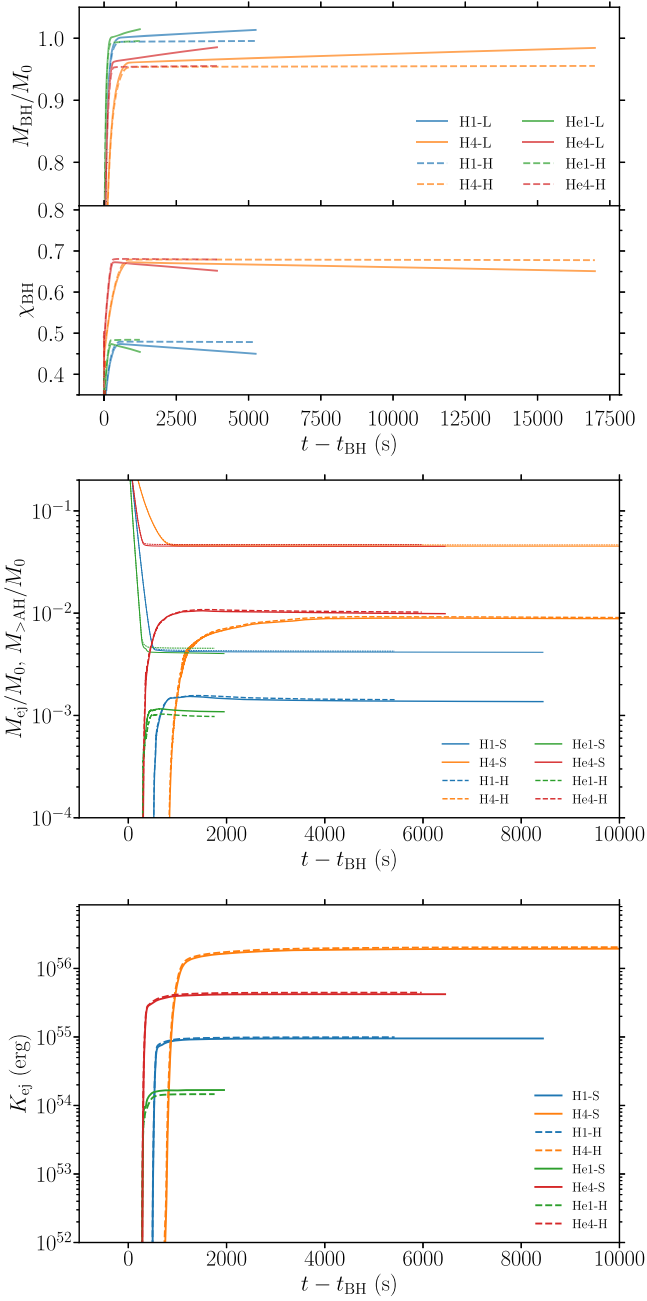


Figure 10. Comparisons of black hole properties (top), ejecta mass relative to the total mass of the star (middle), and ejecta kinetic energy (bottom) between different grid resolutions for models H1, H4, He1, and He4. The standard- and high-resolution results are shown by the solid and dashed curves, respectively. In the middle panel, the rest mass of the matter outside the apparent horizon, $M_{>\text{AH}}$, is also shown in the thin curves.

regridding. The top panel of Figure 10 compares the mass and dimensionless spin of the black hole. The black hole mass in the high-resolution models is systematically lower than that for the corresponding standard-resolution models, while the dimensionless spin of the black hole is systematically higher than that for standard-resolution simulations. The reason for these trends is that the mass and dimensionless spin increase and decrease, respectively, spuriously due to numerical errors, which are suppressed in higher grid resolutions approximately at the fourth order (e.g., S. Fujibayashi et al. 2024). In the present standard-resolution simulations, the black hole horizon

is resolved only by ≈ 15 grid points, and as a result, the black hole mass spuriously increases $\sim 1\%$ over a period of $10^3 GM_{\text{BH}}/c^3$ even without mass accretion. For the high-resolution simulations, the black hole horizon is resolved by ≈ 24 grid points, and thus, the spurious behavior is suppressed by a factor of $\sim (15/24)^4 \approx 0.15$.

The middle and bottom panels of Figure 10 compare the ejecta mass normalized by M_0 and asymptotic kinetic energy of the ejecta. The ejecta mass and kinetic energy tend to be larger for higher-resolution models. This trend is consistent with the smaller mass and the higher dimensionless spin of the formed black hole in higher-resolution models; they result in a smaller radius of the innermost stable circular orbit, and therefore, the torus bounce effect becomes more appreciable.

For models with higher values of $T_{\text{kin}}/|W|$, H4 and He4, the ejecta quantities have no notable dependence on the grid resolution. By contrast, for models H1 and He1, the dependences are clearer in the ejecta mass and kinetic energy simply because the amount of the ejecta mass is relatively small. The differences in the final ejecta mass and kinetic energy are within 30% even in these cases, and hence, the qualitative picture discussed in this paper is not affected by the grid resolution.

4. Discussion

4.1. Property of Ejecta in Realistic Environment

Supermassive stars are likely born in an infalling primordial gas cloud, which is as massive as or more massive than the supermassive star itself (e.g., J. L. Johnson et al. 2013; D. J. Whalen et al. 2013b; and S. J. Patrick et al. 2023). The gas cloud is also likely to be surrounded by a compact halo. The kinetic energy of the ejecta found in the previous section, 10^{55} – 10^{56} erg, can be large enough to engulf such a surrounding massive cloud and a halo, if these are not extremely massive and compact.¹¹ Thus, the contribution of the ejecta originated from the supermassive stellar core is significant only in terms of the kinetic energy, because the mass, expected to be $\sim 1\%$ of the stellar mass, is minor compared to the mass of the cloud and halo.

Supermassive stars in reality may have an inflated envelope with a radius $\sim 10^{15}$ cm because of the high accretion rate, $\gtrsim 0.1 M_{\odot} \text{ yr}^{-1}$ (T. Hosokawa et al. 2013). The more diluted structure of the stellar envelope than those studied in this paper may affect the radial distribution of the ejecta properties shown in Figure 5. Nevertheless, the ejecta is formed in the vicinity of the black hole, and the effects of outer structure on the ejecta kinetic energy are likely to be only minor.

4.2. Electromagnetic Transients Associated with Collapses of Supermassive Stars

The exploded supermassive star inside the primordial (hydrogen-rich) gas cloud may show similar electromagnetic transients to those of Type-IIp supernovae, but scaled up by many orders of magnitude in terms of mass and energy (H. Uchida et al. 2017). Because of the longer diffusion timescale of the ejecta, the transients can last for years in the

¹¹ In J. L. Johnson et al. (2013) and D. J. Whalen et al. (2013b), it is shown that the blast wave generated by an explosion with energy of $\sim 10^{55}$ erg is likely to lose energy by several efficient cooling processes. In their work, the matter swept up by the blast wave is likely to recollapse with a time delay of several 10 Myr. The delay time depends on how dense the cloud is.

rest frame of the explosion. For example, employing a semianalytical model of T. Matsumoto et al. (2016; under the assumption of the primordial composition of the ejecta and Thomson scattering dominated opacity), the bolometric luminosity in the plateau phase reaches its peak at

$$t_{\text{peak}} \approx 10 \text{ yr} \times \left(\frac{r_0}{10^{15} \text{ cm}} \right)^{1/7} \left(\frac{E_{\text{exp}}}{10^{56} \text{ erg}} \right)^{-5/28} \left(\frac{M_{\text{ej}}}{10^5 M_{\odot}} \right)^{15/28} \quad (51)$$

with the peak value of

$$L_{\text{peak}} \approx 3 \times 10^{45} \text{ erg s}^{-1} \times \left(\frac{r_0}{10^{15} \text{ cm}} \right)^{4/7} \left(\frac{E_{\text{exp}}}{10^{56} \text{ erg}} \right)^{11/14} \left(\frac{M_{\text{ej}}}{10^5 M_{\odot}} \right)^{-5/14}, \quad (52)$$

where r_0 , E_{exp} , and M_{ej} denote the supermassive star radius, explosion energy, and ejecta mass (including the contribution from the stellar envelope), respectively.

Optical transients for the thermonuclear explosion of supermassive stars were previously discussed with radiation hydrodynamics simulations in D. J. Whalen et al. (2013a), T. J. Moriya et al. (2021), and C. Nagele et al. (2023b). The electromagnetic feature of the transient expected in our scenario would be similar to them because the composition of the stellar envelope is rich in hydrogen also in their case. The explosion energy found in the present study is about 10 times larger than that found for the thermonuclear explosions (K.-J. Chen et al. 2014b; C. Nagele et al. 2022). Therefore, the transient in the present study would be more luminous than those expected for the results of K.-J. Chen et al. (2014b) and C. Nagele et al. (2022).

The emission could be even brighter and longer lasting in the presence of a surrounding optically thick gas cloud. Hydrodynamics interaction of the ejecta matter with the gas cloud may efficiently convert the ejecta kinetic energy into internal energy and sustain the opacity of ejecta by keeping the temperature above the recombination temperature. If this is the case, a gas cloud with a mass of $M_c = 10^6 M_{\odot}$ and a size of $R_c = 0.3 \text{ pc} \approx 10^{18} \text{ cm}$ heated up by the explosion with the energy of 10^{56} erg can be as bright as

$$L \approx 2 \times 10^{46} \text{ erg s}^{-1} \times \left(\frac{R_c}{10^{18} \text{ cm}} \right) \left(\frac{E_{\text{exp}}}{10^{56} \text{ erg}} \right) \left(\frac{M_c}{10^6 M_{\odot}} \right)^{-1} \quad (53)$$

with the photon diffusion timescale of

$$t_{\text{diff}} \approx 10^2 \text{ yr} \left(\frac{E_{\text{exp}}}{10^{56} \text{ erg}} \right)^{-1/4} \left(\frac{M_c}{10^6 M_{\odot}} \right)^{3/4}. \quad (54)$$

As supermassive stars possibly form and explode in the high-redshift universe, the duration in the observer's frame can be even longer. At the same time, the typical wavelength of the emission is redshifted. For example, if the explosion in the redshift of $z \approx 10$ results in Type-IIp-like emission, the emission in the plateau phase, of which spectra in the source frame may be approximated by a blackbody of the hydrogen recombination temperature ($\approx 6000 \text{ K}$), will be observed in the mid-infrared band of JWST with the duration of

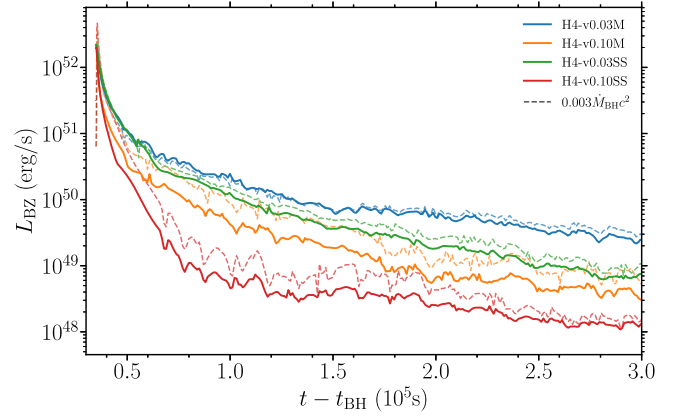


Figure 11. Estimated possible Blandford–Znajek luminosity. The dashed curves denote the rate of the mass accretion onto the black hole multiplied by a constant factor 0.003. See main text in Section 4.2 for the definition.

$\sim (1+z)t_{\text{peak}} \sim 100 \text{ yr}$ or $\sim (1+z)t_{\text{diff}} \sim 10^3 \text{ yr}$. Hence, we may observe such “transients” as red quasi-persistent sources. The observational features will be discussed in detail in our follow-up work (C. Jockel et al. 2025, in preparation).

The mass accretion onto the black hole would lead to other activities. If a sufficient magnetic field accretes onto the black hole in association with mass accretion and a magnetically dominated region, supported by the gas pressure of the torus, is subsequently established around the black hole, the Blandford–Znajek (BZ) process (R. D. Blandford & R. L. Znajek 1977) can extract the rotational energy of the black hole in the form of a Poynting flux. The extracted energy would then form a relativistic jet toward the more evacuated polar directions (T. Matsumoto et al. 2015).

Figure 11 shows the hypothetical BZ luminosity estimated by (M. Shibata et al. 2024)

$$L_{\text{BZ}} \approx 1 \times 10^{49} \text{ erg s}^{-1} \left(\frac{\chi}{0.7} \right)^2 \left(\frac{M_{\text{BH}}}{10^5 M_{\odot}} \right)^2 \left(\frac{B}{3 \times 10^9 \text{ G}} \right)^2, \quad (55)$$

where B denotes the poloidal magnetic flux penetrating the black hole horizon and is estimated assuming that the magnetic pressure is the same as the matter pressure at an innermost region of the torus around the black hole, i.e., $B^2/8\pi = \xi \rho c_s^2|_{\text{ISCO}}$. Here, the value of $\rho c_s^2|_{\text{ISCO}}$ is evaluated at $x = 6GM_0/c^2$ in the equatorial direction, and the factor ξ , which represents the hypothetical saturation level of magnetic energy compared to the internal energy, is set to be 0.1. The shape of the luminosity curve resembles the mass accretion rate (top panel of the same figure), with the efficiency defined by $L_{\text{BZ}}/M_c c^2$ of ~ 0.003 . If the Poynting flux is assumed to be continuously emitted for the viscous timescale of the torus, the total energy generated by this process is $\sim 10^{55} \text{ erg}$ for H4 models. The hypothetical collimated energy injection into the possibly inflated stellar envelope and the gas cloud, which would surround the supermassive star, may form a cocoon, which emits thermal photons when it breaks out from the surface of the star or the cloud (K. Kashiyama et al. 2013; D. Nakauchi et al. 2013). Thus, the jet may also play an important role for the possible electromagnetic signals.

4.3. Possible Qualitative Differences from Collapses of Usual Massive Stars

For the collapse of rotating supermassive stars, we observe that the bounce of the torus drives an outflow. Contrary to that, in gravitational collapses of stars of mass $\sim 10\text{--}100M_{\odot}$, such a strong bounce and corresponding outflow are not found in the latest numerical simulations (e.g., O. Just et al. 2022; C. Dean & R. Fernández 2024; S. Fujibayashi et al. 2024).

The difference between the collapses associated with the usually massive and supermassive stars may lie in the unstable mode that triggers their collapses. The collapse of the supermassive stars is triggered by the general relativistic instability, in which the star is unstable with respect to the radial fundamental perturbation of no node (S. Chandrasekhar 1964). This indicates that all the stellar matter starts collapsing coherently. As a result, the torus formation proceeds rather coherently after the black hole formation, enhancing a strong bounce on the torus surface, and furthermore, the density outside the torus becomes very low at their formation; this is preferable for the subsequent prompt shock propagation.

On the other hand, the collapses of usual massive stars are induced by the electron capture and/or photodissociation of heavy nuclei, or the thermal production of $e^{-}e^{+}$ pairs at their center. Because these processes are active only around the central region of the star with high density and temperature, the unstable region is restricted compared to the entire star. As a result, only the central region starts collapsing earlier, and the outer envelope is still in hydrostatic equilibrium at the onset of the central collapse. The matter in the outer region starts collapsing when it loses the pressure support from the inside of the star, typically after the sound-crossing time of the star. When a torus is formed around the black hole, there is still significant matter infalling to the center, which exerts a large ram pressure to prohibit the immediate launch of the bounce-induced outflow (e.g., S. Fujibayashi et al. 2024).

For the supermassive star cores with the mass lower than those investigated in this paper, $\lesssim 10^4M_{\odot}$, the density and temperature of the torus would be higher, and hence, several processes may play an important role in decreasing the pressure of the downstream region of the shock, in the same way for the core-bounce after the proton-neutron star formation (e.g., H.-T. Janka 2012 for a review): e.g., the photodissociation of heavy nuclei converts the internal energy into the rest mass. In addition, the emitted neutrinos carry the internal energy away from the bounced matter. The importance of such effects in the context of the bounce of the torus is worth investigating for the collapse of low-mass supermassive star cores.

4.4. Effect of Further Nuclear Burning and Prospects of Lower-mass Stars

For the models studied in this paper, the nuclear burning plays a negligible role for the dynamics, because the rate of hydrogen burning is limited by the temperature-independent hot CNO cycle, and the triple- α reaction is an inefficient process. However, after the carbon is synthesized, the $^{12}\text{C}(\alpha, \gamma)^{16}\text{O}$ reaction will take place, and further energy generation may be possible. In K.-J. Chen et al. (2014b) and C. Nagele et al. (2020), the further nuclear burning indeed synthesizes heavier species up to ^{28}Si . The feedback due to such energy generation is not taken into account in our present

work. In particular, for the collapse of helium-burning supermassive star cores, such effects may be important.

There are other possible channels of the supermassive star formation in which the composition of the star is not necessarily primordial (M. Gieles et al. 2018; L. Mayer & S. Bonoli 2019). In this case, the CNO cycle is more efficient to burn hydrogen in the collapse of the supermassive star, which is more likely to explode by the nuclear energy generation (K. J. Fricke 1973; G. M. Fuller et al. 1986; C. Nagele et al. 2023a; see also M. Shibata et al. 2025 for discussion).

A supermassive star with a lower final mass will have a lower-entropy core, which has a higher density than that investigated in this work for a given value of temperature. The gravitational collapse (due to the onset of either general relativistic or pair-production instability) of such a lower-mass star will occur in a later evolution stage, i.e., in a later phase of helium burning or after the core helium depletion (e.g., M. Shibata et al. 2025). For the collapse of such a star, further nuclear burning and its back-reactions to the dynamics may be more significant. To address such possibilities, the current hydrodynamics has to be coupled with a more sophisticated nuclear reaction network (e.g., the networks in K.-J. Chen et al. 2014b; C. Nagele et al. 2020).

4.5. Neutrino Cooling

H. Uchida et al. (2017) showed that the neutrino emission plays a negligible role after the black hole formation for models that are essentially the same as ours. In this subsection, we consider the model He4, which results in the highest-density and highest-temperature torus, and hence, the neutrino cooling has the most significant effects among the models considered in this paper. In the following, we will show that the entropy change by the neutrino emission is negligible even for this model. The neutrino luminosity is $\sim 10^{48}\text{ erg s}^{-1}$ after the black hole formation for the model He4 (see Figure 7 in H. Uchida et al. 2017). The rate of total entropy extraction by neutrino emission can be estimated as

$$\dot{S}/k_{\text{B}} \sim -\frac{L_{\nu}}{k_{\text{B}}T} \approx -7 \times 10^{55} \text{ s}^{-1} \left(\frac{L_{\nu}}{10^{48} \text{ erg s}^{-1}} \right) \left(\frac{T}{10^8 \text{ K}} \right)^{-1}. \quad (56)$$

On the other hand, the total entropy of the torus is

$$S/k_{\text{B}} \approx 3.7 \times 10^{63} \left(\frac{s_{\text{torus}}/k_{\text{B}}}{380} \right) \left(\frac{M_{\text{torus}}}{8000M_{\odot}} \right), \quad (57)$$

where the values of entropy per baryon and torus mass are taken from the results for model He4. The timescale of the change in the entropy is thus estimated as $S/|\dot{S}| \approx 5 \times 10^7 \text{ s}$ for this model. As the bounce process occurs in a much shorter timescale of $< 10^3 \text{ s}$, the neutrino cooling can be safely ignored.

For lower-mass supermassive star cores with masses of $\lesssim 10^4M_{\odot}$, the neutrino cooling may have more significant effects, as the density and temperature become higher. To investigate the outcomes of such stars, we have to include the cooling by various neutrino emission processes (e.g., those mentioned in N. Itoh et al. 1996).

4.6. Possible Path to Supermassive Black Holes

A black hole formed from a supermassive star core of mass $\sim 10^5M_{\odot}$ may be surrounded by a dense cloud of mass much

larger than that of the supermassive star, say $10^7 M_\odot$ (S. J. Patrick et al. 2023). Suppose that the gas cloud is not entirely blown off by the explosion from the torus surrounding the formed black hole. Then, after the black hole formation, a super Eddington mass accretion onto the central black hole may continue because the typical mass accretion rate onto supermassive stars during their growth is $\sim 0.1 M_\odot \text{ yr}^{-1}$, which is $\sim 10^2$ times higher than the Eddington accretion rate for the $10^5 M_\odot$ black hole (J. L. Johnson et al. 2013; D. J. Whalen et al. 2013b). Recent numerical simulations (e.g., Y.-F. Jiang et al. 2014; H. Hu et al. 2022) demonstrate that, even for such a very high mass accretion rate, a fraction (an order of 10%) of the matter still falls into the black hole, although a significant fraction of the infalling matter is outflowed from the system. Hence, a super Eddington accretion growth of the black hole could follow after the formation of a massive black hole from the supermassive stars. This suggests that a black hole formed from a supermassive star with mass $\sim 10^5 M_\odot$ may subsequently rapidly grow, leading to a supermassive black hole of mass $\gtrsim 10^6 M_\odot$ in $\sim 10^8 \text{ yr}$, which has been observed in the high-redshift universe by JWST (Y. Harikane et al. 2023; V. Kokorev et al. 2023; R. L. Larson et al. 2023; H. Übler et al. 2023; R. Maiolino et al. 2024). Developing a scenario that connects supermassive star formation, collapse to a seed massive black hole, and subsequent rapid growth of it will be interesting issues to be explored.

5. Summary

In this work, we performed general relativistic hydrodynamics simulations of the collapses of rotating supermassive star cores to investigate the properties of the ejecta as an extension of the previous work (H. Uchida et al. 2017). We took into account an approximate nuclear burning up to carbon, as in the previous work, and in addition, we incorporated a detailed equation of state, for which ions, photons, electrons, and thermally generated e^-e^+ pairs are taken into account.

For all the models we investigated, the energy generation by nuclear burning plays only a minor role, leading to the formation of a black hole without an explosion via nuclear burning. However, for rotating models, the stellar explosion sets in from the accreting torus, which forms after the formation of the black hole, with explosion energies up to 10^{-4} times the mass–energy of the supermassive star cores. We found that, even if we increased the rotation of the progenitor, the ejecta mass saturates at $\sim 1\%$ of the total mass of the initial star. The average ejecta velocity also saturates at $\approx 0.2c$. As a result, the ejecta kinetic energy is approximately proportional to the initial mass of the star.

We further performed viscous hydrodynamics simulations after the black hole and torus formation. We found that, because of the relatively small velocity ($\approx 0.07c$) of the viscosity-driven ejecta, its effect is subdominant in terms of the kinetic energy, although an appreciable fraction of the torus matter can be ejected by this process.

The collapse of a supermassive star is likely to occur in a dense atomic cooling gas cloud as massive as or more massive than the supermassive star itself, according to its formation scenario. As the ejecta mass is minor compared to the mass of the hosting cloud, the explosion plays a role in injecting the kinetic energy into the cloud. It may be observed as a very long-duration supernova-like transient. As it likely occurs in a high-redshift ($z \gtrsim 10$) universe and the observational duration

can be extended by the cosmological redshift effect, we may observe it as a quasi-persistent source. A detail of our analysis on this will be presented in a separate paper (C. Jockel et al. 2025, in preparation).

The mass accretion of the black hole via the formed torus may also drive a relativistic jet via the BZ process. This outflow may inject energy comparable to that of the ejecta driven by the bounce of the torus. Such an additional energy injection may be important for the electromagnetic signals. We plan to study this process in future work.

Acknowledgments

We thank Jan-Torge Schindler, Takashi Hosokawa, Koh Takahashi, Kohei Inayoshi, Shigeo Kimura, and Kazumi Kashiyama for stimulating discussions. This work was in part supported by Grant-in-Aid for Scientific Research (grant Nos. 20H00158 and 23H04900) of Japanese MEXT/JSPS. Numerical computations were performed at Sakura of the Max Planck Computing and Data Facility.

Appendix A Electron Equation of State

In this appendix, we summarize the detailed implementation of the electron contribution to the equation of state. The internal energy density and pressure of electrons and e^-e^+ pairs are determined by the net electron number density n_e and temperature T . We prepare a two-dimensional table of the internal energy per electric charge

$$\tilde{\epsilon}_e(\rho Y_e, T) = \frac{e_e}{\rho Y_e}, \quad (\text{A1})$$

where we used $m_e n_e = \rho Y_e$ instead of n_e for a later convenience. In the same manner, P_e is tabulated as a function of ρY_e and T . In our implementation, we use the equation of state by F. X. Timmes et al. (2000) to construct the table of $\tilde{\epsilon}_e$ and P_e as functions of ρY_e and T . For a given ρ , T , and Y_e , we first interpolate $\tilde{\epsilon}_e$ and P_e from the table with $(\rho Y_e, T)$. Then, the specific internal energy of electrons is calculated by

$$\epsilon_e(\rho, T, Y_e) = Y_e \tilde{\epsilon}_e(\rho Y_e, T). \quad (\text{A2})$$

Appendix B Sound Speed

To solve hydrodynamics numerically, we need the sound speed. In this appendix, we present a way to calculate the sound speed if there are several contributions, a part of which is obtained by interpolating equation of state tables. Suppose that there are no changes of $\langle A \rangle$, $\langle \Delta m \rangle$, and Y_e : we may then write the variation of the pressure in terms of the variations of ρ and ϵ as

$$\begin{aligned} dP &= \left(\frac{\partial P}{\partial \rho} \right)_\epsilon d\rho + \left(\frac{\partial P}{\partial \epsilon} \right)_\rho d\epsilon \\ &= \left(\frac{\partial P}{\partial \rho} \right)_\epsilon d\rho + \left(\frac{\partial P}{\partial \epsilon} \right)_\rho \left(T ds + \frac{P}{\rho^2} d\rho \right), \end{aligned} \quad (\text{B1})$$

where the first law of thermodynamics was used in the second line. In the equation above and in the rest of this appendix, we fix Y_e in the partial derivatives without writing it explicitly. In a similar way, from this expression, the sound speed is then

written as

$$hc_s^2 = \left(\frac{\partial P}{\partial \rho} \right)_s = \frac{P}{\rho^2} \left(\frac{\partial P}{\partial \varepsilon} \right)_\rho + \left(\frac{\partial P}{\partial \rho} \right)_\varepsilon, \quad (\text{B2})$$

where $h = 1 + \varepsilon/c^2 + P/\rho c^2$ is the specific enthalpy. It is beneficial if there is a way to describe the sound speed using the derivatives of thermodynamical quantities with respect to T and ρ , which are the usual inputs of equations of state. From an expression of ε as a function of ρ and T , and the first law of thermodynamics, we have

$$d\varepsilon = \left(\frac{\partial \varepsilon}{\partial \rho} \right)_T d\rho + \left(\frac{\partial \varepsilon}{\partial T} \right)_\rho dT = Tds + \frac{P}{\rho^2} d\rho. \quad (\text{B3})$$

In the above, the temperature T is expressed as a function of s and ρ . Then,

$$\begin{aligned} dP &= \left(\frac{\partial P}{\partial \rho} \right)_T d\rho + \left(\frac{\partial P}{\partial T} \right)_\rho dT \\ &= \left(\frac{\partial P}{\partial \rho} \right)_T d\rho + \left(\frac{\partial P}{\partial T} \right)_\rho \left(\frac{\partial \varepsilon}{\partial T} \right)_\rho^{-1} \\ &\quad \times \left[Tds + \left(\frac{P}{\rho^2} - \left(\frac{\partial \varepsilon}{\partial \rho} \right)_T \right) d\rho \right]. \end{aligned}$$

The last expression indicates the sound speed as

$$hc_s^2 = \left(\frac{\partial P}{\partial \rho} \right)_T + \left(\frac{\partial P}{\partial T} \right)_\rho \left(\frac{\partial \varepsilon}{\partial T} \right)_\rho^{-1} \left[\frac{P}{\rho^2} - \left(\frac{\partial \varepsilon}{\partial \rho} \right)_T \right]. \quad (\text{B4})$$

For our physical ingredients, we have

$$\left(\frac{\partial P}{\partial \rho} \right)_T = \frac{k_B T}{\langle A \rangle m_u} + \left(\frac{\partial P_e}{\partial \rho} \right)_T, \quad (\text{B5})$$

$$\left(\frac{\partial P}{\partial T} \right)_\rho = \frac{4}{3} a_{\text{rad}} T^3 + \frac{\rho k_B}{\langle A \rangle m_u} + \left(\frac{\partial P_e}{\partial T} \right)_\rho, \quad (\text{B6})$$

$$\left(\frac{\partial \varepsilon}{\partial \rho} \right)_T = -\frac{a_{\text{rad}} T^4}{\rho^2} + \left(\frac{\partial \varepsilon_e}{\partial \rho} \right)_T, \quad (\text{B7})$$

$$\left(\frac{\partial \varepsilon}{\partial T} \right)_\rho = \frac{4a_{\text{rad}} T^3}{\rho} + \frac{3}{2} \frac{k_B}{\langle A \rangle m_u} + \left(\frac{\partial \varepsilon_e}{\partial T} \right)_\rho. \quad (\text{B8})$$

Again, P_e and $\varepsilon_e = Y_e \tilde{\varepsilon}_e$ are functions of ρY_e and T . Their partial derivatives with respect to T are calculated trivially as

$$\left(\frac{\partial P_e}{\partial T} \right)_\rho = \frac{\partial P_e(\rho Y_e, T)}{\partial T} \Big|_{\rho Y_e}, \quad (\text{B9})$$

$$\left(\frac{\partial \varepsilon_e}{\partial T} \right)_\rho = \frac{\partial}{\partial T} (Y_e \tilde{\varepsilon}_e(\rho Y_e, T)) \Big|_{\rho Y_e} = Y_e \frac{\partial \tilde{\varepsilon}_e}{\partial T} \Big|_{\rho Y_e}. \quad (\text{B10})$$

The derivatives with respect to ρ (fixing Y_e) are more complicated as

$$\left(\frac{\partial P_e}{\partial \rho} \right)_T = \frac{\partial(\rho Y_e)}{\partial \rho} \frac{\partial P_e(\rho Y_e, T)}{\partial(\rho Y_e)} \Big|_T = Y_e \frac{\partial P_e}{\partial(\rho Y_e)} \Big|_T, \quad (\text{B11})$$

$$\left(\frac{\partial \varepsilon_e}{\partial \rho} \right)_T = Y_e \frac{\partial(\rho Y_e)}{\partial \rho} \frac{\partial \tilde{\varepsilon}_e(\rho Y_e, T)}{\partial(\rho Y_e)} \Big|_T = Y_e^2 \frac{\partial \tilde{\varepsilon}_e}{\partial(\rho Y_e)} \Big|_T. \quad (\text{B12})$$

In our implementation, we also use Timmes equation of state to tabulate $\partial P_e / \partial(\rho Y_e)|_T$, $\partial P_e / \partial T|_{\rho Y_e}$, $\partial \tilde{\varepsilon}_e / \partial(\rho Y_e)|_T$, and $\partial \tilde{\varepsilon}_e / \partial T|_{\rho Y_e}$

as functions of $(T, \rho Y_e)$, and interpolate them to a given set of (ρ, T, Y_e) to calculate the sound speed with Equation (B4).

Appendix C Neutrino Scattering

In this appendix, we justify our assumption of completely ignoring the scattering processes of neutrinos. As the typical energy of the emitted electron-type neutrinos is 1 MeV, the scattering by the electrons and nuclei is the main process to prevent neutrinos from free-streaming. The cross sections of these processes with neutrino energy of ~ 1 MeV are $\sim 10^{44}$ cm². Thus, the neutrino optical depth of the supermassive star core at the onset of the collapse is approximately evaluated as

$$\begin{aligned} \tau_{c0} &\sim \sigma_{\text{scat}} \frac{\rho_{c,0}}{m_u} R_{e,0} \\ &\approx 6 \times 10^{-8} \left(\frac{\sigma_{\text{scat}}}{10^{-44} \text{ cm}^2} \right) \left(\frac{\rho_{c,0}}{1 \text{ g cm}^{-3}} \right) \left(\frac{R_{e,0}}{10^{13} \text{ cm}} \right), \quad (\text{C1}) \end{aligned}$$

where $\rho_{c,0}$ is the central rest-mass density of the initial, marginally stable supermassive star core, listed in Table 1. This very low optical depth suggests that we can ignore the neutrino interactions at the initial stage of the collapse. As the collapse proceeds, the column density of the star, and hence the optical depth, increases. Because the supermassive star core collapses coherently, the radius of the core is approximately proportional to $\rho_c^{-1/3}$. Thus, the optical depth increases in proportion to $\rho_c^{2/3}$. Figure 1 shows that the central density increases by 6–7 orders of magnitude before the black hole formation. Hence, the optical depth at the black hole formation, $\tau_{c,\text{BH}}$, can be estimated as

$$\begin{aligned} \tau_{c,\text{BH}} &\sim \sigma_{\text{scat}} \frac{\rho_c R_e}{m_u} \\ &\approx 0.003 \left(\frac{\sigma_{\text{scat}}}{10^{-44} \text{ cm}^2} \right) \left(\frac{\rho_{c,0}}{1 \text{ g cm}^{-3}} \right) \left(\frac{R_{e,0}}{10^{13} \text{ cm}} \right) \left(\frac{\rho_{c,\text{BH}}/\rho_{c,0}}{10^7} \right)^{2/3}, \quad (\text{C2}) \end{aligned}$$

where $\rho_{c,\text{BH}}$ is the central density of the collapsing supermassive star core at the black hole formation. Because the neutrino optical depth is much smaller than unity even at the black hole formation, at which the optical depth is the highest, we can safely ignore the neutrino interaction after its emission.

ORCID iDs

Sho Fujibayashi  <https://orcid.org/0000-0001-6467-4969>
Cédric Jockel  <https://orcid.org/0009-0007-7617-7178>
Kyohei Kawaguchi  <https://orcid.org/0000-0003-4443-6984>
Yuichiro Sekiguchi  <https://orcid.org/0000-0002-2648-3835>
Masaru Shibata  <https://orcid.org/0000-0002-4979-5671>

References

- Alcubierre, M., Brügmann, B., Holz, D., et al. 2001, *IJMPD*, 10, 273
Alvarez, M. A., Wise, J. H., & Abel, T. 2009, *ApJL*, 701, L133
Arnowitz, R., Deser, S., & Misner, C. W. 1960, *PhRv*, 118, 1100
Balbus, S. A., & Hawley, J. F. 1991, *ApJ*, 376, 214
Balbus, S. A., & Hawley, J. F. 1998, *RvMP*, 70, 1
Baumgarte, T. W., & Shapiro, S. L. 1998, *ApJ*, 504, 431
Baumgarte, T. W., Shapiro, S. L., & Shibata, M. 2000, *ApJL*, 528, L29
Blandford, R. D., & Znajek, R. L. 1977, *MNRAS*, 179, 433
Bogdán, Á., Goulding, A. D., Natarajan, P., et al. 2024, *NatAs*, 8, 126
Bond, J. R., Arnett, W. D., & Carr, B. J. 1984, *ApJ*, 280, 825

- Bromm, V., & Loeb, A. 2003, *ApJ*, **596**, 34
- Campanelli, M., Lousto, C. O., Marronetti, P., & Zlochower, Y. 2006, *PhRvL*, **96**, 111101
- Chandrasekhar, S. 1964, *ApJ*, **140**, 417
- Chen, K.-J., Heger, A., Woosley, S., Almgren, A., & Whalen, D. J. 2014a, *ApJ*, **792**, 44
- Chen, K.-J., Heger, A., Woosley, S., et al. 2014b, *ApJ*, **790**, 162
- Chon, S., Hirano, S., Hosokawa, T., & Yoshida, N. 2016, *ApJ*, **832**, 134
- Dean, C., & Fernández, R. 2024, *PhRvD*, **109**, 083010
- Fan, X., Bañados, E., & Simcoe, R. A. 2023, *ARA&A*, **61**, 373
- Fricke, K. J. 1973, *ApJ*, **183**, 941
- Fujibayashi, S., Lam, A. T.-L., Shibata, M., & Sekiguchi, Y. 2024, *PhRvD*, **109**, 023031
- Fujibayashi, S., Sekiguchi, Y., Kiuchi, K., & Shibata, M. 2017, *ApJ*, **846**, 114
- Fujibayashi, S., Shibata, M., Wanajo, S., et al. 2020a, *PhRvD*, **101**, 083029
- Fujibayashi, S., Shibata, M., Wanajo, S., et al. 2020b, *PhRvD*, **102**, 123014
- Fujibayashi, S., Takahashi, K., Sekiguchi, Y., & Shibata, M. 2021, *ApJ*, **919**, 80
- Fujibayashi, S., Wanajo, S., Kiuchi, K., et al. 2020c, *ApJ*, **901**, 122
- Fuller, G. M., Woosley, S. E., & Weaver, T. A. 1986, *ApJ*, **307**, 675
- Gieles, M., Charbonnel, C., Krause, M. G. H., et al. 2018, *MNRAS*, **478**, 2461
- Goulding, A. D., Greene, J. E., Setton, D. J., et al. 2023, *ApJL*, **955**, L24
- Haemmerlé, L., Woods, T. E., Klessen, R. S., Heger, A., & Whalen, D. J. 2018, *ApJL*, **853**, L3
- Harikane, Y., Zhang, Y., Nakajima, K., et al. 2023, *ApJ*, **959**, 39
- Hilditch, D., Bernuzzi, S., Thierfelder, M., et al. 2013, *PhRvD*, **88**, 084057
- Hirano, S., Hosokawa, T., Yoshida, N., & Kuiper, R. 2017, *Sci*, **357**, 1375
- Hirano, S., Hosokawa, T., Yoshida, N., et al. 2014, *ApJ*, **781**, 60
- Hosokawa, T., Yorke, H. W., Inayoshi, K., Omukai, K., & Yoshida, N. 2013, *ApJ*, **778**, 178
- Hu, H., Inayoshi, K., Haiman, Z., Quataert, E., & Kuiper, R. 2022, *ApJ*, **934**, 132
- Inayoshi, K., & Omukai, K. 2012, *MNRAS*, **422**, 2539
- Inayoshi, K., Visbal, E., & Haiman, Z. 2020, *ARA&A*, **58**, 27
- Itoh, N., Hayashi, H., Nishikawa, A., & Kohyama, Y. 1996, *ApJS*, **102**, 411
- Janka, H.-T. 2012, *ARNPS*, **62**, 407
- Jiang, Y.-F., Stone, J. M., & Davis, S. W. 2014, *ApJ*, **796**, 106
- Johnson, J. L., & Bromm, V. 2007, *MNRAS*, **374**, 1557
- Johnson, J. L., Whalen, D. J., Even, W., et al. 2013, *ApJ*, **775**, 107
- Just, O., Aloy, M. A., Obergaulinger, M., & Nagataki, S. 2022, *ApJL*, **934**, L30
- Kashiyama, K., Nakauchi, D., Suwa, Y., Yajima, H., & Nakamura, T. 2013, *ApJ*, **770**, 8
- Kimura, K., Hosokawa, T., Sugimura, K., & Fukushima, H. 2023, *ApJ*, **950**, 184
- Kippenhahn, R., & Weigert, A. 1990, *Stellar Structure and Evolution* (Berlin: Springer)
- Kiuchi, K., Sekiguchi, Y., Shibata, M., & Taniguchi, K. 2009, *PhRvD*, **80**, 064037
- Kokorev, V., Fujimoto, S., Labbe, I., et al. 2023, *ApJL*, **957**, L7
- Kovács, O. E., Bogdán, Á., Natarajan, P., et al. 2024, *ApJL*, **965**, L21
- Larson, R. L., Finkelstein, S. L., Kocevski, D. D., et al. 2023, *ApJL*, **953**, L29
- Lee, H., & Yoon, S.-C. 2016, *ApJ*, **820**, 135
- Lee, W. H., & Ramirez-Ruiz, E. 2006, *ApJ*, **641**, 961
- Liu, Y. T., Shapiro, S. L., & Stephens, B. C. 2007, *PhRvD*, **76**, 084017
- Maeder, A., & Meynet, G. 2000, *A&A*, **361**, 159
- Maiolino, R., Scholtz, J., Curtis-Lake, E., et al. 2024, *A&A*, **691**, A145
- Matsumoto, T., Nakauchi, D., Ioka, K., Heger, A., & Nakamura, T. 2015, *ApJ*, **810**, 64
- Matsumoto, T., Nakauchi, D., Ioka, K., & Nakamura, T. 2016, *ApJ*, **823**, 83
- Mayer, L., & Bonoli, S. 2019, *RPPH*, **82**, 016901
- Milosavljević, M., Couch, S. M., & Bromm, V. 2009, *ApJL*, **696**, L146
- Montero, P. J., Janka, H.-T., & Müller, E. 2012, *ApJ*, **749**, 37
- Moriya, T. J., Chen, K.-J., Nakajima, K., Tominaga, N., & Blinnikov, S. I. 2021, *MNRAS*, **503**, 1206
- Moriya, T. J., Harikane, Y., & Inoue, A. K. 2023, *MNRAS*, **526**, 2400
- Nagele, C., & Umeda, H. 2024, *PhRvD*, **110**, L061301
- Nagele, C., Umeda, H., & Takahashi, K. 2023a, *MNRAS*, **523**, 1629
- Nagele, C., Umeda, H., Takahashi, K., & Maeda, K. 2023b, *MNRAS*, **520**, L72
- Nagele, C., Umeda, H., Takahashi, K., Yoshida, T., & Sumiyoshi, K. 2020, *MNRAS*, **496**, 1224
- Nagele, C., Umeda, H., Takahashi, K., Yoshida, T., & Sumiyoshi, K. 2022, *MNRAS*, **517**, 1584
- Nakauchi, D., Kashiyama, K., Suwa, Y., & Nakamura, T. 2013, *ApJ*, **778**, 67
- Omukai, K. 2001, *ApJ*, **546**, 635
- Patrick, S. J., Whalen, D. J., Latif, M. A., & Elford, J. S. 2023, *MNRAS*, **522**, 3795
- Rees, M. J. 1978, *Obs*, **98**, 210
- Saio, H., Nandal, D., Ekström, S., & Meynet, G. 2024, *A&A*, **689**, A169
- Sekiguchi, Y. 2010, *PThPh*, **124**, 331
- Shakura, N. I., & Sunyaev, R. A. 1973, *A&A*, **500**, 33
- Shen, K. J., & Bildsten, L. 2007, *ApJ*, **660**, 1444
- Shibata, M. 2000, *PThPh*, **104**, 325
- Shibata, M. 2016, *Numerical Relativity* (Singapore: World Scientific)
- Shibata, M., Fujibayashi, S., Jockel, C., & Kawaguchi, K. 2025, *ApJ*, **978**, 58
- Shibata, M., Fujibayashi, S., Lam, A. T.-L., Ioka, K., & Sekiguchi, Y. 2024, *PhRvD*, **109**, 043051
- Shibata, M., Kiuchi, K., Sekiguchi, Y., & Suwa, Y. 2011, *PThPh*, **125**, 1255
- Shibata, M., Kiuchi, K., & Sekiguchi, Y.-i. 2017, *PhRvD*, **95**, 083005
- Shibata, M., & Nakamura, T. 1995, *PhRvD*, **52**, 5428
- Shibata, M., & Sekiguchi, Y. 2012, *PThPh*, **127**, 535
- Shibata, M., & Shapiro, S. L. 2002, *ApJL*, **572**, L39
- Shibata, M., Uchida, H., & Sekiguchi, Y.-i. 2016, *ApJ*, **818**, 157
- Thorne, K. S. 1981, *MNRAS*, **194**, 439
- Timmes, F. X., & Arnett, D. 1999, *ApJS*, **125**, 277
- Timmes, F. X., Hoffman, R. D., & Woosley, S. E. 2000, *ApJS*, **129**, 377
- Timmes, F. X., & Swesty, F. D. 2000, *ApJS*, **126**, 501
- Toyouchi, D., Inayoshi, K., Li, W., Haiman, Z., & Kuiper, R. 2023, *MNRAS*, **518**, 1601
- Übler, H., Maiolino, R., Curtis-Lake, E., et al. 2023, *A&A*, **677**, A145
- Uchida, H., Shibata, M., Yoshida, T., Sekiguchi, Y., & Umeda, H. 2017, *PhRvD*, **96**, 083016
- Umeda, H., Hosokawa, T., Omukai, K., & Yoshida, N. 2016, *ApJL*, **830**, L34
- Volonteri, M., Habouzit, M., & Colpi, M. 2021, *NatRP*, **3**, 732
- Waxman, E., & Shvarts, D. 1993, *PhFA*, **5**, 1035
- Whalen, D., van Veelen, B., O'Shea, B. W., & Norman, M. L. 2008, *ApJ*, **682**, 49
- Whalen, D. J., Even, W., Smidt, J., et al. 2013a, *ApJ*, **778**, 17
- Whalen, D. J., Johnson, J. L., Smidt, J., et al. 2013b, *ApJ*, **777**, 99
- Wiescher, M., Görres, J., & Schatz, H. 1999, *JPhG*, **25**, R133
- Wise, J. H., Regan, J. A., O'Shea, B. W., et al. 2019, *Natur*, **566**, 85